

CH₃CCH as a thermometer in warm molecular gas

YUQIANG LI ,^{1,2,3,4,*} JUNZHI WANG ,^{5,†} JUAN LI ,^{1,4,‡} XING LU ,¹ SIQI ZHENG ,^{1,3,6,4} CHAO OU ,⁵
 QIAN HUANG,⁵ MIGUEL SANTANDER-GARCÍA ,^{7,8} JOSÉ JAIRO DÍAZ-LUIS ,^{7,8} SEOKHO LEE ,² TIE LIU ,¹ AND
 ZHIQIANG SHEN 

¹Shanghai Astronomical Observatory, Chinese Academy of Sciences, No. 80 Nandan Road, Shanghai, 200030, People's Republic of China
²Korea Astronomy and Space Science Institute, No. 776, Daedeok-daero, Yuseong-gu, Daejeon, Republic of Korea

³School of Astronomy and Space Sciences, University of Chinese Academy of Sciences, No. 19A Yuquan Road, Beijing 100049, People's Republic of China

⁴State Key Laboratory of Radio Astronomy and Technology, A20 Datun Road, Chaoyang District, Beijing, 100101, P. R. China

⁵Guangxi Key Laboratory for Relativistic Astrophysics, Department of Physics, Guangxi University, Nanning 530004, People's Republic of China

⁶I. Physikalisches Institut, Universität zu Köln, Zülpicher Str. 77, 50937 Köln, Germany

⁷Observatorio Astronómico Nacional (OAN, IGN), C/ Alfonso XII 3, 28014 Madrid, Spain

⁸Observatorio de Yebes (IGN). Cerro de la Palera s/n, 19141 Yebes, Guadalajara, Spain

ABSTRACT

Kinetic temperature is a fundamental parameter in molecular clouds. Symmetric top molecules, such as NH₃ and CH₃CCH, are often used as thermometers. However, at high temperatures, NH₃(2,2) can be collisionally excited to NH₃(2,1) and rapidly decay to NH₃(1,1), which can lead to an underestimation of the kinetic temperature when using rotation temperatures derived from NH₃(1,1) and NH₃(2,2). In contrast, CH₃CCH is a symmetric top molecule with lower critical densities of its rotational levels than those of NH₃, which can be thermalized close to the kinetic temperature at relatively low densities of about 10⁴ cm⁻³. To compare the rotation temperatures derived from NH₃(1,1)&(2,2) and CH₃CCH rotational levels in warm molecular gas, we used observational data toward 55 massive star-forming regions obtained with Yebes 40m and TMRT 65m. Our results show that rotation temperatures derived from NH₃(1,1)&(2,2) are systematically lower than those from CH₃CCH 5-4. This suggests that CH₃CCH rotational lines with the same $J+1 \rightarrow J$ quantum number may be a more reliable thermometer than NH₃(1,1)&(2,2) in warm molecular gas located in the surroundings of massive young stellar objects or, more generally, in massive star-forming regions.

Keywords: stars: massive — stars: formation — ISM: molecules

1. INTRODUCTION

Kinetic temperature is one of the key parameters in molecular clouds (Evans 1999). It significantly influences the chemical evolution of molecular clouds (Caselli & Ceccarelli 2012), as it regulates gas-phase reaction rates (e.g., Wakelam et al. 2010; Garrod et al. 2008) and release of molecules from icy mantles into the gas phase (e.g., Viti & Williams 1999; Garrod et al. 2008; Herbst & van Dishoeck 2009), thereby determining which chemical pathways dominate (e.g., Garrod & Herbst 2006; Kaiser et al. 2015; Hacar et al. 2020). Consequently, variations in kinetic temperature, together with other factors such as gas density, radiation field, metallicity, and cosmic-ray ionization rate, strongly affect the relative abundances of complex organic and simple species in star-forming regions. In addition, the kinetic temperature is a key factor in the star formation process, as it controls the balance between thermal pressure and gravity, thereby influencing the fragmentation of molecular clouds and the formation of dense cores (e.g., Bergin & Tafalla 2007; McKee & Ostriker 2007; Gieser et al. 2023; Schinnerer & Leroy 2024). Accurate measurements of this

* E-mail: lyq@kasi.re.kr

† E-mail: junzhiwang@gxu.edu.cn

‡ E-mail: lijuan@shao.ac.cn

parameter are essential for understanding the physical and chemical environments of the interstellar medium (ISM; e.g., Evans 1999; McKee & Ostriker 2007; Jørgensen et al. 2020).

Carbon monoxide (CO) and its isotopologues, mainly ^{13}CO , emission are widely used to estimate gas temperature under the assumptions of local thermodynamic equilibrium (LTE) and optically thick conditions (Nagahama et al. 1998). But the rotation transitions of CO often suffer from self-absorption effects, which can lead to inaccurate estimates of the gas temperature (e.g., Castets et al. 1990; Mazumdar et al. 2021; Park et al. 2023). Slightly asymmetric top molecules, such as formaldehyde (H_2CO , Mangum & Wootten 1993), are considered a thermometer due to their nearly symmetric structures, which make their rotational level populations sensitive to kinetic temperature (e.g., Mundy et al. 1987; Mangum & Wootten 1993; Tang et al. 2018; Zhao et al. 2024). However, H_2CO is difficult to thermalize in most of the molecular clouds, because of its relatively high critical density ($\sim 10^6 \text{ cm}^{-3}$, Guzmán et al. 2011; Feng et al. 2019). Accurate temperature determination using H_2CO requires non-LTE radiative transfer modeling (e.g., Mangum & Wootten 1993; Tang et al. 2017, 2021; Mendoza et al. 2023; Gerin et al. 2024; Huang et al. 2025), which involves many input parameters (such as gas density, background radiation temperature and source geometry) and introduces considerable uncertainties in the derived kinetic temperatures.

Symmetric top molecules, such as ammonia (NH_3 , Ho & Townes 1983), acetonitrile (CH_3CN , Askne et al. 1984) and methyl acetylene (CH_3CCH , Bergin et al. 1994), are a class of molecules characterized by having a rotational symmetry axis. Their rotational energy levels are described by two quantum numbers: J , representing the total angular momentum, and K , the projection of J along the symmetry axis (Townes & Schawlow 1955; Fontani et al. 2002; Giannetti et al. 2017). Because the dipole moment of symmetric top molecules is parallel to the symmetry axis, the radiative transitions between different K levels are forbidden and the relative populations of different K levels are only related to collisions (e.g., Townes & Schawlow 1955; Cheung et al. 1969; Bauer et al. 1979). These molecules follow specific selection rules for rotational transitions: $\Delta J = \pm 1$ and $\Delta K = 0$. Because the energy differences between the same $J+1 \rightarrow J$ transitions in different K -ladders are similar, while the corresponding upper-state energies (E_u) differ significantly (such as CH_3CCH , see Figure 1), symmetric top molecules can exhibit multiple transitions, with same $J+1 \rightarrow J$ and different K , at closely spaced frequencies (Bergin et al. 1994). These characteristics make them particularly effective thermometers in the ISM, as the relative intensities of these transitions are highly sensitive to the kinetic temperature.

For NH_3 , energy levels with $J > K$ are referred to as non-metastable, while those with $J = K$ are called metastable (Ho & Townes 1983). The dipole moment of NH_3 is approximately 1.47 D (Tanaka et al. 1987). The non-metastable levels require very high critical densities ($\sim 10^8\text{-}10^9 \text{ cm}^{-3}$) to be excited, causing them to decay rapidly via $\Delta J = 1$ transitions until they stabilize in a metastable state (Ho & Townes 1983). Metastable levels undergo only inversion transitions ($\Delta J = 0$, $\Delta K = 0$), which are produced by rapid vibrations of NH_3 , allowing its nitrogen atom to tunnel quantum-mechanically through the plane of the three hydrogen atoms, resulting in microwave inversion transitions (see Townes & Schawlow 1955, chap. 12). Among these levels, $\text{NH}_3(1,1)$ and $\text{NH}_3(2,2)$ are often used to derive the kinetic temperature. The excitation between sub-levels of inversion transitions within metastable levels requires much lower critical densities ($\sim 10^3\text{-}10^4 \text{ cm}^{-3}$), making transitions such as $\text{NH}_3(1,1)$ and $\text{NH}_3(2,2)$ widely used to study physical conditions in star-forming regions at different evolutionary stages, from infrared dark clouds (IRDCs; e.g., Benson & Myers 1989; Wienen et al. 2012; Lu et al. 2014) to hot molecular cores (e.g., Wienen et al. 2012; Li et al. 2016a) and ultracompact H II regions (e.g., Urquhart et al. 2011; Wienen et al. 2012; Urquhart et al. 2015). However, as temperature increases, $\text{NH}_3(2,2)$ can be collisionally excited to the non-metastable $\text{NH}_3(2,1)$, which can rapidly decay to $\text{NH}_3(1,1)$ (Cheung et al. 1969). Consequently, at temperatures above ~ 25 K, the populations of $\text{NH}_3(1,1)$ and $\text{NH}_3(2,2)$ no longer reliably reflect the kinetic temperature, limiting their effectiveness as thermometers (Walmsley & Ungerechts 1983; Tafalla et al. 2004).

In contrast, CH_3CCH has a relatively small electric dipole moment ($\mu=0.78$ D, Bauer et al. (1979)), allowing its rotational transitions to be easily thermalized at densities $n \gtrsim 10^4 \text{ cm}^{-3}$ (Askne et al. 1984; Fontani et al. 2002; Molinari et al. 2016). In addition, the energy level differences for $\Delta J = 1$ transitions in CH_3CCH are smaller than those of NH_3 , making all transitions of CH_3CCH more easily excited in the ISM. At millimeter and submillimeter wavelengths, the $J+1 \rightarrow J$ transitions of CH_3CCH exhibit several K -ladder components at nearly the same frequencies, which can be observed simultaneously and reduce the uncertainties from telescope calibration and pointing. Because of these properties, CH_3CCH is an excellent thermometer in molecular clouds (e.g., Giannetti et al. 2017; Calcutt et al. 2019; Lin et al. 2022), better than $\text{NH}_3(1,1)$ and $\text{NH}_3(2,2)$ in warm molecular gas.

Over the past decade, several observational studies used NH₃, CH₃CN, and CH₃CCH as temperature tracers in various star-forming environments, ranging from IRDCs to hot cores (e.g., Molinari et al. 2016; Giannetti et al. 2017; Calcutt et al. 2019; Lin et al. 2022). These different molecular thermometers probe distinct gas components depending on density and excitation conditions (e.g., Giannetti et al. 2017; Tang et al. 2018; Zhao et al. 2024). However, systematic comparisons between temperatures derived from CH₃CCH and NH₃ using uniform samples remain limited. Since, as pointed out in Tafalla et al. (2004), NH₃(1,1)&(2,2) are primarily sensitive to relatively low temperatures (\lesssim 20-25 K), it is useful to compare the rotation temperatures derived from NH₃(1,1)&(2,2) with those obtained from a more reliable thermometer in warm gas. Therefore, we compare two approaches for calculating rotation temperatures, one using CH₃CCH $J=5-4$ and the other using NH₃(1,1)&(2,2).

Using Yebes 40m telescope and Shanghai Tianma 65m radio telescope (TMRT) observations, this work presents a comparison of rotation temperatures derived from CH₃CCH $J=5-4$ and NH₃(1,1)&(2,2) toward a sample of late-stage massive star-forming regions. These targets are associated with 6.7 GHz CH₃OH maser emission (Reid et al. 2014), indicating the presence of warm gas with kinetic temperatures of 20-100 K (Bergin & Tafalla 2007; Torstensson et al. 2011). The observations are described in Section 2, the methods used to derive the rotation temperatures of CH₃CCH are given in Section 3, the main results are presented in Section 4, the discussion is given in Section 5, and a brief summary is given in Section 6.

2. OBSERVATIONS AND DATA REDUCTION

The Yebes 40m radio telescope was used to observe CH₃CCH $J=5-4$ at 85457.3003 MHz toward 101 massive star-forming regions with 6.7 GHz CH₃OH masers, using the same sample as Reid et al. (2014). The details of each source are listed in Table 1. The position-switch mode was used in our observations with a frequency coverage of about 18.5 GHz bandwidth, spanning from 72 to 90.5 GHz. The Fast Fourier Transform Spectrometer (XFFTS) was used with 65536 channels, corresponding to a frequency resolution of 38 kHz and a velocity resolution of 0.13 km s⁻¹ at 85 GHz. The system temperatures ranged from 110 to 390 K. The beam size of Yebes 40m is about 20.5'' at 86.2 GHz. In the following analysis, the velocity resolution is smoothed to about 0.6 km s⁻¹ with a frequency resolution of 153 kHz at 85457.3003 MHz. The typical rms was about 15 mK (T_{A}^* scale) at 0.6 km s⁻¹ velocity resolution.

CH₃CCH 5-4 was detected in 55 targets, which showed distinct CH₃CCH ($J=5-4$, $K=2$) emissions above the 3σ level. Among these, 18 sources have previously reported NH₃(1,1) and NH₃(2,2) observations with the Effelsberg 100m telescope (Li et al. 2016a), and the reported data are used in this work. The TMRT 65m was used to observe NH₃(1,1) and NH₃(2,2) toward the remaining 37 targets. Observations were conducted in the digital backend system (DIBAS, Li et al. 2016b) mode 6, with 131072 channels and a bandwidth of 187.5 MHz, providing a frequency resolution of 1.4 kHz and a velocity resolution of 0.02 km s⁻¹ at about 23.7 GHz. The position-switch mode was also used during TMRT observations. The beam size of TMRT is about 50'' at 23 GHz. The system temperatures were 100-200 K during our observation. In the following analysis, the velocity resolution was also smoothed to about 0.6 km s⁻¹, with a frequency resolution of 46 kHz at 23694.4955 MHz. The typical rms was about 20 mK (T_{A}^* scale) at 0.6 km s⁻¹ velocity resolution. The main beam efficiency of the Yebes 40m telescope varies by less than 0.1% between 85431.1745 MHz (corresponding $K=4$ line) to 85457.3003 MHz (corresponding to $K=0$ line)¹ (Tercero et al. 2021). Applying the main beam efficiency correction would only rescale the line intensities, affecting the derived column densities but leaving the relative line ratios unchanged. As a result, the derived rotation temperature is not affected. Because our primary aim is to determine T_{rot} rather than absolute column densities, no main-beam efficiency correction was applied to the spectra before the fitting.

Data reduction was conducted with CLASS/GILDAS software². First-order baselines were used for all spectra. The T_{A}^* scale was used for all spectra instead of the T_{mb} scale because only the intensity ratios were needed and the frequencies of the line for calculating ratios are close. In the following analysis, we assume that the beam-filling factor is unity.

3. CH₃CCH SPECTRAL FITTING

The rotation temperature of CH₃CCH 5-4 ($T_{\text{rot}}(\text{CH}_3\text{CCH})$) was obtained by directly fitting the observed spectra with a multi-Gaussian model under the assumption of LTE. The modeled spectra were generated using spectroscopic

¹ https://rt40m.oan.es/rt40m_en.php

² <http://www.iram.fr/IRAMFR/GILDAS>

parameters (line frequencies, Einstein coefficients, upper state energy and upper state degeneracy) by CDMS³ (Müller et al. 2001, 2005). For each source, the Local Standard of Rest velocity (v_{lsr}), rotation temperature (T_{rot}), Full Width at Half Maximum (FWHM), and column density are treated as global free parameters and are shared by all the K components. Each K component is modeled as a Gaussian line profile, assuming that all K levels are optically thin. Synthetic spectra were compared with the observations using the non-linear least-squares minimization routine *curve_fit* from *scipy.optimize* module⁴ (Virtanen et al. 2020). The best-fit T_{rot} values were determined by minimizing the residuals between the observed and modeled spectra, and the parameter uncertainties were estimated from the covariance matrix returned by the fit.

4. RESULTS

4.1. Rotation temperature of CH₃CCH

The CH₃CCH ($J=5-4$, $K=2$) transition was detected above the 3σ level in 55 out of 101 targets observed with the Yebes 40m telescope. As shown in Table 2, the detected $K=2$ component of CH₃CCH spans a sufficiently wide range in energy to allow the determination of the rotation temperature (Goldsmith & Langer 1999; Mangum & Shirley 2015). Although the $K=3$ transition of CH₃CCH 5-4 was detected in 36 sources with 3σ level, only $K=0,1,2$ transitions of CH₃CCH 5-4 were used in the spectra fitting to maintain a uniform analysis. An example of the CH₃CCH 5-4 fitting result for G005.88-00.39 is presented in Figure 2a, while the results for other sources are shown in Figure B1-B5. The derived $T_{\text{rot}}(\text{CH}_3\text{CCH})$ are listed in Table 3. Some of our sources (e.g., G012.80-00.20, G028.86+00.06, and G035.19-00.74) were also reported by Giannetti et al. (2017), who obtained rotation temperature of CH₃CCH from a simultaneous fit of the 5-4, 6-5, and 20-19 transitions, yielding results consistent with this work.

4.2. Statistical equilibrium calculation of CH₃CCH

We solved the statistical equilibrium equations for CH₃CCH using level energy (E_i), level degeneracy (g_i), Einstein emission coefficient (A_{ij}) and collisional rate coefficients (C_{ij}) provided by Ben Khalifa et al. (2024). Ben Khalifa et al. (2024) provided the collisional data for CH₃CCH-He, and the He→H₂ scaling from excitation of molecules and atoms for astrophysics database (EMAA)⁵ was applied following (Faure et al. 2025) to obtain H₂ collision data. The level populations were determined by solving:

$$\sum_{j \neq i} n_j (C_{ij} + R_{ij}) - n_i \sum_{j \neq i} (C_{ij} + R_{ij}) = 0, \quad (1)$$

where C_{ij} is the collisional rates, R_{ij} is radiative rates and n_i is population of level i . We approximate the radiative rates by retaining only spontaneous emission,

$$R_{ij} \simeq \begin{cases} A_{ij}, & E_i > E_j \text{ (downward)} \\ 0, & E_i < E_j \text{ (upward)} \end{cases} \quad (2)$$

i.e., we neglect stimulated emission and radiative absorption. For missing reverse collisional rate coefficients, we used detailed balance:

$$C_{ji} = C_{ij} \frac{g_i}{g_j} \exp\left[-\frac{E_i - E_j}{kT_{\text{kin}}}\right], \quad (3)$$

where k is the Boltzmann constant and T_{kin} is kinetic temperature. Populations were normalized such that $\sum_i n_i = 1$ when solving Eq. 1.

Using these models to predict the population of $J=5-4$, $K=0,1,2,3,4$ transitions, we can obtain the $T_{\text{rot}}(\text{CH}_3\text{CCH})$ as a function of both gas density and kinetic temperature. Figure 3 shows the results of the statistical equilibrium calculations, which are consistent with those reported by Bergin et al. (1994). When density exceeds 10^4 cm^{-3} , the derived T_{rot} approaches the kinetic temperature T_{kin} , indicating that the CH₃CCH levels are nearly thermalized under such conditions. In our sample of 55 targets with detected CH₃CCH ($J=5-4$, $K=2$) emission, the H¹³CN 1-0 was also detected, which has a critical density of about $9 \times 10^5 \text{ cm}^{-3}$ at 20 K, calculated using $n_{\text{crit}} = A_{ij}/C_{ij}$, where the Einstein emission coefficient and collisional rate coefficients are taken from the EMAA database. Therefore, T_{kin} can be reliably traced by $T_{\text{rot}}(\text{CH}_3\text{CCH})$ in these sources.

³ <https://cdms.astro.uni-koeln.de/classic/predictions/catalog/>

⁴ <https://scipy.org>

⁵ <https://emaa.osug.fr>

4.3. Rotation temperature of NH₃

Among these 55 targets, 18 have previously reported rotation temperatures of NH₃ ($T_{\text{rot}}(2,2;1,1)$), derived from the NH₃(1,1) and (2,2) inversion transitions, and denoted as $T_{\text{rot}}(\text{NH}_3)$) with Effelsberg 100m observations (Li et al. 2016a), which were used in this work. To ensure consistency, three of the sources from Li et al. (2016a) were also observed with the TMRT. The rotation temperatures of NH₃ derived from TMRT observations are 19.3 ± 0.5 K, 23.9 ± 0.5 K, and 24.3 ± 0.3 K in G081.75+00.59, G109.87+02.11 and G111.54+00.77, respectively. For comparison, the corresponding values reported by Li et al. (2016a) are 18.5 ± 0.3 K, 23.4 ± 3.0 K and 26.0 ± 1.7 K, respectively. The results demonstrate good consistency between the TMRT and Effelsberg observations.

For the remaining 37 targets, ammonia inversion transitions NH₃(1,1) and NH₃(2,2) were observed using TMRT. In these 37 targets, NH₃(1,1) absorption was detected in three sources, G010.62-00.38, G012.80-00.20 and G133.94+01.06, which were also reported by Keto et al. (1988), Tursun et al. (2022) and Reid et al. (1987), respectively. Additionally, both NH₃(1,1) and NH₃(2,2) exhibit a low signal-to-noise ratio in G209.00-19.38. For this source, the rms noise is 12 mK at a velocity resolution of 0.6 km s⁻¹, and the NH₃ hyperfine components are below the 3σ level, resulting in unreliable hyperfine fitting and temperature determination. Excluding these four sources, a total of 33 sources with TMRT observations were used in this work.

Based on the theoretical frameworks of Ho & Townes (1983) and Mangum et al. (1992), Lu et al. (2015) provided a Python code⁶ to fit the NH₃(1,1) and NH₃(2,2) spectra to derive $T_{\text{rot}}(2,2;1,1)$. Within this framework, the NH₃(1,1) and NH₃(2,2) lines are fitted simultaneously, assuming Gaussian profiles for all hyperfine structure components. For each source, five parameters are treated as free parameters in the fitting, including $T_{\text{rot}}(2,2;1,1)$, $\tau(1,1,m)$, column density ($N_{\text{tot}}(\text{NH}_3)$), v_{LSR} and FWHM. The $T_{\text{rot}}(2,2;1,1)$, $N_{\text{tot}}(\text{NH}_3)$, v_{LSR} and FWHM are assumed to be the same for all hyperfine components, while $\tau(1,1,m)$ is determined from the relative intensities of the NH₃(1,1) hyperfine structure and is used to correct for opacity effects. Using this code, the $T_{\text{rot}}(2,2;1,1)$ derived from the relative populations of the NH₃(1,1) and NH₃(2,2) was obtained for 33 sources observed with TMRT. One of the fitting results for G005.88-00.39 is presented in Figure 2b, while other sources are shown in Figure C1-C3.

4.4. Compare the rotation temperature of CH₃CCH and NH₃

The range of $T_{\text{rot}}(\text{CH}_3\text{CCH})$ spans from 23.0 ± 0.4 K to 88.8 ± 3.0 K, while $T_{\text{rot}}(2,2;1,1)$ ranges from 15.7 ± 0.4 K to 29.5 ± 0.6 K. The highest value of optical depth for the NH₃(1,1) main group observed by TMRT is 2.9, which is detected in G012.90-00.24. The median value of $T_{\text{rot}}(\text{CH}_3\text{CCH})$ is 33.1 ± 0.6 K, while $T_{\text{rot}}(2,2;1,1)$ is 20.7 ± 0.5 K. A comparison of the rotation temperatures derived from CH₃CCH 5-4 and NH₃(1,1)&(2,2) is presented in Figure 4. For most sources, $T_{\text{rot}}(\text{CH}_3\text{CCH})$ is significantly higher than that obtained from NH₃(1,1)&(2,2) at temperatures higher than 30 K.

5. DISCUSSION

We compare the rotation temperature derived from CH₃CCH 5-4 and NH₃(1,1)&NH₃(2,2) in late-stage massive star-forming regions to investigate the physical origin of their differences and to evaluate that CH₃CCH is a more reliable thermometer than NH₃ in warm gas. The excitation properties and temperature sensitivities of these two tracers have been described in Section 1. Almost all targets show that $T_{\text{rot}}(\text{CH}_3\text{CCH})$ is higher than $T_{\text{rot}}(2,2;1,1)$, which may help to illustrate the underlying causes of this difference.

As shown in Figure 4, the range of $T_{\text{rot}}(\text{CH}_3\text{CCH})$ is significantly broader than that of $T_{\text{rot}}(2,2;1,1)$. As $T_{\text{rot}}(\text{CH}_3\text{CCH})$ increases, $T_{\text{rot}}(2,2;1,1)$ shows insignificant increase. When T_{kin} is above 20 K, $T_{\text{rot}}(2,2;1,1)$ is not sensitive to temperature, indicating that the empirical equation between the $T_{\text{rot}}(2,2;1,1)$ and the T_{kin} (e.g., Estalella 2017; Swift et al. 2005; Tafalla et al. 2004) may also not provide accurate kinetic temperature of NH₃. This suggests that NH₃ may not be a reliable thermometer in warm molecular gas.

With the statistical equilibrium calculations, Walmsley & Ungerechts (1983) reported that $T_{\text{rot}}(2,2;1,1)$ deviates from T_{kin} as the temperature increases. Tafalla et al. (2004) improved this method with Monte Carlo models to estimate T_{kin} from $T_{\text{rot}}(2,2;1,1)$ as a function almost independent of density:

$$T_{\text{kin}} = \frac{T_{\text{rot}}(2,2;1,1)}{1 - \frac{T_{\text{rot}}(2,2;1,1)}{\Delta E(2,2;1,1)} \ln[1 + 1.1 \exp(\frac{-16}{T_{\text{rot}}(2,2;1,1)})]}, \quad (4)$$

⁶ <https://github.com/xinglunju/pyAmor>

where $\Delta E(2, 2; 1, 1) = [E(2, 2) - E(1, 1)]/k$ is the temperature associated with energy level difference. However, [Tafalla et al. \(2004\)](#) also pointed out that the uncertainty of this function becomes significant when $T_{\text{kin}} > 20$ K (see the green line in Figure 4). As shown by the statistical equilibrium calculation in Section 4.2, our targets can be reasonably assumed to follow $T_{\text{kin}} = T_{\text{rot}}(\text{CH}_3\text{CCH})$. In all targets, the $T_{\text{rot}}(\text{CH}_3\text{CCH})$ is higher than 20 K, while $T_{\text{rot}}(2, 2; 1, 1)$ is lower than the T_{kin} derived from NH_3 in almost all targets, particularly when $T_{\text{rot}}(\text{CH}_3\text{CCH})$ exceeds 30 K. This indicates that T_{kin} cannot be reliably predicted from $T_{\text{rot}}(2, 2; 1, 1)$ at higher temperatures, as $T_{\text{rot}}(2, 2; 1, 1)$ loses sensitivity to temperature variations. An accurate estimation of temperature from NH_3 may require higher- J metastable transitions, such as $\text{NH}_3(4, 4)$ and $\text{NH}_3(5, 5)$. But these transitions are hard to detect in most molecular clouds, because they need higher excitation temperatures. Therefore, when using $\text{NH}_3(1, 1)$ and $\text{NH}_3(2, 2)$ as a thermometer in warm molecular gas one should be cautious.

Compared to NH_3 , CH_3CCH is more easily thermalized at gas density $n \gtrsim 10^4 \text{ cm}^{-3}$ ([Askne et al. 1984](#)). Statistical equilibrium calculations by [Bergin et al. \(1994\)](#) and Section 4.2 further demonstrated that the rotation temperature of CH_3CCH closely approximates the kinetic temperature at gas density $n \gtrsim 10^4 \text{ cm}^{-3}$. Therefore, CH_3CCH is a reliable tracer of kinetic temperature in warm gas of star-forming regions.

A wide range of rotational transitions of CH_3CCH have been used to derive kinetic temperatures of molecular clouds. Transitions in the 3 mm and 2 mm bands, such as $J=5-4$, $J=6-5$, $J=8-7$ and $J=9-8$ are often used (e.g., [Churchwell & Hollis 1983](#); [Bergin et al. 1994](#); [Giannetti et al. 2017](#); [Pazukhin et al. 2023](#)). These mid- J lines cover E_u in the range of $\sim 10\text{--}100$ K across their first four K -levels, making them ideal for tracing kinetic temperatures in warm gas ($T=20\text{--}100$ K). Higher- J transitions ($J > 11$), whose $K=0$ levels have E_u exceeding 50 K, are suitable for probing hotter environments ($T > 50$ K, e.g., [Calcutt et al. 2019](#); [Lin et al. 2022](#); [Santos et al. 2022](#)). Although $J=3-2$, $J=4-3$, $J=7-6$ and $J=11-10$ transitions are in principle accessible, they are seldom used. Because $J=3-2$, $J=7-6$, and $J=11-10$ transitions lie in frequency ranges with very poor atmospheric transmission, the $J=4-3$ transition lies close to an atmospheric window and can only be observed under exceptionally good conditions. The $J=1-0$ transition is useless for temperature estimation because it includes only the $K=0$ line, while the $J=2-1$ transitions are also rarely used in warm molecular gas, as the energy difference between $K=0$ and $K=1$ levels is 7.2 K, making it insensitive to excitation conditions. However, the $J=2-1$ transitions might be used to derive kinetic temperatures in cold environments ($T \lesssim 20$ K), with a similar usable range to that of $T_{\text{rot}}(2, 2; 1, 1)$ for NH_3 .

CH_3CN , as another symmetric top molecule, had been more widely used as a thermometer than CH_3CCH , because of relatively strong emission ([Askne et al. 1984](#)) with a larger dipole moment ($\mu=3.922$ D; [Gadhi et al. 1995](#)). The properties of CH_3CN and CH_3CCH are very similar. The two species share many physical similarities: both are symmetric top molecules with nearly identical rotational energy structures consisting of multiple K -components within each J -transition, and both can be used to estimate gas temperatures. In addition, the separations between K -levels in CH_3CCH and CH_3CN are similar, which allows temperature diagnostics over a broad range of physical conditions. A comparison of the two molecules was reported by [Giannetti et al. \(2017\)](#). They derived rotation temperatures of CH_3CCH and CH_3CN toward a large sample of ATLASGAL sources. They found that $T_{\text{rot}}(\text{CH}_3\text{CN})$ is systematically higher than $T_{\text{rot}}(\text{CH}_3\text{CCH})$, suggesting that CH_3CCH traces the cooler, more extended envelope gas, while CH_3CN probes the denser and warmer cores. This result highlights their complementary diagnostic power in probing different temperature conditions of star-forming regions. However, the relatively strong emission of CH_3CN means that the low K levels are often optically thick ([Zhang et al. 1998](#)). Moreover, CH_3CN is typically concentrated in the immediate vicinity of protostellar objects, tracing more compact and warmer regions than CH_3CCH ([Bisschop et al. 2008](#)). In this case, CH_3CN cannot provide an accurate kinetic temperature in molecular clouds, while CH_3CCH is still a reliable thermometer because of its relatively low optical depth for low K level lines. Another disadvantage of CH_3CN lines is the higher critical densities of $J > K$ levels as non-metastable ones than those of CH_3CCH , because the dipole moment of CH_3CN is about 5 times greater than that of CH_3CCH .

Considering the presence of temperature gradients in massive star-forming regions (e.g., [Dewangan et al. 2015](#); [Li et al. 2003](#); [Schneider et al. 2010](#)), CH_3CCH and NH_3 may trace different regions within the envelope ([Giannetti et al. 2017](#)). It could be one of the reasons for the significant discrepancies observed between the rotation temperatures derived from CH_3CCH and NH_3 in our sources. This requires spatially resolved information of CH_3CCH and NH_3 for further analysis. Additionally, the beam sizes for these two molecules differ in the present work. Specifically, the beam size of Yebes 40m is about $20.5''$ at 86.2 GHz, while the beam sizes of TMRT and Effelsberg are $50''$ and $43''$ at 23 GHz, respectively. The larger beam sizes of NH_3 observations may have included more lower-temperature gas from the residual envelope, resulting in $T_{\text{rot}}(\text{CH}_3\text{CCH})$ being higher than $T_{\text{rot}}(2, 2; 1, 1)$. In addition, the heliocentric

distances of our targets range from 0.7 to 10.2 kpc, corresponding to physical sizes from 0.07 to 1.02 pc assuming a 20.5'' beam size. This indicates that the derived rotational temperatures may represent averages over different spatial scales. Therefore, using observations with similar beam sizes of CH₃CCH and NH₃ toward sample sources with similar distances may provide a more reliable comparison of these two temperature tracers. Overall, our results reinforce previous theoretical predictions that CH₃CCH traces the warm gas more reliably than NH₃(1,1)&(2,2), and the rotation temperature difference can be attributed to the collisional excitation of NH₃ into non-metastable levels at higher kinetic temperatures.

6. CONCLUSIONS

Using Yebes 40m and TMRT 65m observations, we investigate CH₃CCH and NH₃ as temperature tracers in warm molecular gas. We find that the $T_{\text{rot}}(\text{CH}_3\text{CCH})$ is significantly higher than $T_{\text{rot}}(2,2;1,1)$. This discrepancy may arise because NH₃ accumulates in the (1,1) level at high temperatures, leading to an underestimation of the kinetic temperature. Our results suggest that CH₃CCH provides a more reliable and sensitive probe of gas temperature than NH₃(1,1)&(2,2), particularly in warm molecular regions with $T_{\text{kin}} > 20$ K. Caution should be taken when using $T_{\text{rot}}(2,2;1,1)$ in such environments.

This work is supported by the National Key R&D Program of China (No. 2022YFA1603101) and the National Natural Science Foundation of China (NSFC, Grant No. 12173067). This work is also supported by 100101 Key Laboratory of Radio Astronomy and Technology (Chinese Academy of Sciences). X.Lu acknowledges support from the Strategic Priority Research Program of the Chinese Academy of Sciences (CAS) Grant No. XDB0800300, State Key Laboratory of Radio Astronomy and Technology (CAS), the National Natural Science Foundation of China (NSFC) through grant Nos. 12273090 and 12322305, the National Science Foundation of Shanghai (No. 23ZR1482100), and the CAS “Light of West China” Program No. xbzg-zdsys-202212. Based on observations carried out with the Yebes 40 m telescope (project code 23A013). The 40 m radio telescope at Yebes Observatory is operated by the Spanish Geographic Institute (IGN; Ministerio de Transportes y Movilidad Sostenible). We thank the support from operators and staff at the TMRT during our observations. S. Zheng would like to thank the China Scholarship Council (CSC) for support. This research has made use of spectroscopic and collisional data from the EMAA database (<https://emaa.osug.fr> and <https://dx.doi.org/10.17178/EMAA>).

REFERENCES

Askne, J., Hoglund, B., Hjalmarson, A., & Irvine, W. M. 1984, A&A, 130, 311

Bauer, A., Boucher, D., Burie, J., Demaison, J., & Dubrulle, A. 1979, Journal of Physical and Chemical Reference Data, 8, 537, doi: [10.1063/1.555603](https://doi.org/10.1063/1.555603)

Ben Khalifa, M., Darna, B., & Loreau, J. 2024, A&A, 683, A53, doi: [10.1051/0004-6361/202348717](https://doi.org/10.1051/0004-6361/202348717)

Benson, P. J., & Myers, P. C. 1989, ApJS, 71, 89, doi: [10.1086/191365](https://doi.org/10.1086/191365)

Bergin, E. A., Goldsmith, P. F., Snell, R. L., & Ungerechts, H. 1994, ApJ, 431, 674, doi: [10.1086/174518](https://doi.org/10.1086/174518)

Bergin, E. A., & Tafalla, M. 2007, ARA&A, 45, 339, doi: [10.1146/annurev.astro.45.071206.100404](https://doi.org/10.1146/annurev.astro.45.071206.100404)

Bisschop, S. E., Jørgensen, J. K., Bourke, T. L., Bottinelli, S., & van Dishoeck, E. F. 2008, A&A, 488, 959, doi: [10.1051/0004-6361:200809673](https://doi.org/10.1051/0004-6361:200809673)

Calcutt, H., Willis, E. R., Jørgensen, J. K., et al. 2019, A&A, 631, A137, doi: [10.1051/0004-6361/201936323](https://doi.org/10.1051/0004-6361/201936323)

Caselli, P., & Ceccarelli, C. 2012, A&A Rv, 20, 56, doi: [10.1007/s00159-012-0056-x](https://doi.org/10.1007/s00159-012-0056-x)

Castets, A., Duvert, G., Dutrey, A., et al. 1990, A&A, 234, 469

Cheung, A. C., Rank, D. M., Townes, C. H., Knowles, S. H., & Sullivan, III, W. T. 1969, ApJL, 157, L13, doi: [10.1086/180374](https://doi.org/10.1086/180374)

Churchwell, E., & Hollis, J. M. 1983, ApJ, 272, 591, doi: [10.1086/161322](https://doi.org/10.1086/161322)

Dewangan, L. K., Luna, A., Ojha, D. K., et al. 2015, ApJ, 811, 79, doi: [10.1088/0004-637X/811/2/79](https://doi.org/10.1088/0004-637X/811/2/79)

Estalella, R. 2017, PASP, 129, 025003, doi: [10.1088/1538-3873/129/972/025003](https://doi.org/10.1088/1538-3873/129/972/025003)

Evans, Neal J., I. 1999, ARA&A, 37, 311, doi: [10.1146/annurev.astro.37.1.311](https://doi.org/10.1146/annurev.astro.37.1.311)

Faure, A., Bacmann, A., & Jacquot, R. 2025, A&A, 700, A266, doi: [10.1051/0004-6361/202554403](https://doi.org/10.1051/0004-6361/202554403)

Feng, S., Caselli, P., Wang, K., et al. 2019, *ApJ*, 883, 202, doi: [10.3847/1538-4357/ab3a42](https://doi.org/10.3847/1538-4357/ab3a42)

Fontani, F., Cesaroni, R., Caselli, P., & Olmi, L. 2002, *A&A*, 389, 603, doi: [10.1051/0004-6361:20020579](https://doi.org/10.1051/0004-6361:20020579)

Gadhi, J., Lahrouni, A., Legrand, J., & Demaison, J. 1995, *J. Chim. Phys.*, 92, 1984, doi: [10.1051/jcp/1995921984](https://doi.org/10.1051/jcp/1995921984)

Garrod, R. T., & Herbst, E. 2006, *A&A*, 457, 927, doi: [10.1051/0004-6361:20065560](https://doi.org/10.1051/0004-6361:20065560)

Garrod, R. T., Widicus Weaver, S. L., & Herbst, E. 2008, *ApJ*, 682, 283, doi: [10.1086/588035](https://doi.org/10.1086/588035)

Gerin, M., Liszt, H., Pety, J., & Faure, A. 2024, *A&A*, 686, A49, doi: [10.1051/0004-6361/202449152](https://doi.org/10.1051/0004-6361/202449152)

Giannetti, A., Leurini, S., Wyrowski, F., et al. 2017, *A&A*, 603, A33, doi: [10.1051/0004-6361/201630048](https://doi.org/10.1051/0004-6361/201630048)

Gieser, C., Beuther, H., Semenov, D., et al. 2023, *A&A*, 674, A160, doi: [10.1051/0004-6361/202245249](https://doi.org/10.1051/0004-6361/202245249)

Goldsmith, P. F., & Langer, W. D. 1999, *ApJ*, 517, 209, doi: [10.1086/307195](https://doi.org/10.1086/307195)

Guzmán, V., Pety, J., Goicoechea, J. R., Gerin, M., & Roueff, E. 2011, *A&A*, 534, A49, doi: [10.1051/0004-6361/201117257](https://doi.org/10.1051/0004-6361/201117257)

Hacar, A., Bosman, A. D., & van Dishoeck, E. F. 2020, *A&A*, 635, A4, doi: [10.1051/0004-6361/201936516](https://doi.org/10.1051/0004-6361/201936516)

Herbst, E., & van Dishoeck, E. F. 2009, *ARA&A*, 47, 427, doi: [10.1146/annurev-astro-082708-101654](https://doi.org/10.1146/annurev-astro-082708-101654)

Ho, P. T. P., & Townes, C. H. 1983, *ARA&A*, 21, 239, doi: [10.1146/annurev.aa.21.090183.001323](https://doi.org/10.1146/annurev.aa.21.090183.001323)

Huang, K.-Y., Behrens, E., Bouvier, M., et al. 2025, *A&A*, 699, A70, doi: [10.1051/0004-6361/202554156](https://doi.org/10.1051/0004-6361/202554156)

Jørgensen, J. K., Belloche, A., & Garrod, R. T. 2020, *ARA&A*, 58, 727, doi: [10.1146/annurev-astro-032620-021927](https://doi.org/10.1146/annurev-astro-032620-021927)

Kaiser, R. I., Parker, D. S. N., & Mebel, A. M. 2015, *Annual Review of Physical Chemistry*, 66, 43, doi: [10.1146/annurev-physchem-040214-121502](https://doi.org/10.1146/annurev-physchem-040214-121502)

Keto, E. R., Ho, P. T. P., & Haschick, A. D. 1988, *ApJ*, 324, 920, doi: [10.1086/165949](https://doi.org/10.1086/165949)

Li, D., Goldsmith, P. F., & Menten, K. 2003, *ApJ*, 587, 262, doi: [10.1086/368078](https://doi.org/10.1086/368078)

Li, F. C., Xu, Y., Wu, Y. W., et al. 2016a, *AJ*, 152, 92, doi: [10.3847/0004-6256/152/4/92](https://doi.org/10.3847/0004-6256/152/4/92)

Li, J., Shen, Z.-Q., Wang, J., et al. 2016b, *ApJ*, 824, 136, doi: [10.3847/0004-637X/824/2/136](https://doi.org/10.3847/0004-637X/824/2/136)

Li, Y., Wang, J., Li, J., et al. 2024, *MNRAS*, 527, 5049, doi: [10.1093/mnras/stad3480](https://doi.org/10.1093/mnras/stad3480)

Lin, Y., Wyrowski, F., Liu, H. B., et al. 2022, *A&A*, 658, A128, doi: [10.1051/0004-6361/202142023](https://doi.org/10.1051/0004-6361/202142023)

Lu, X., Zhang, Q., Liu, H. B., Wang, J., & Gu, Q. 2014, *ApJ*, 790, 84, doi: [10.1088/0004-637X/790/2/84](https://doi.org/10.1088/0004-637X/790/2/84)

Lu, X., Zhang, Q., Wang, K., & Gu, Q. 2015, *ApJ*, 805, 171, doi: [10.1088/0004-637X/805/2/171](https://doi.org/10.1088/0004-637X/805/2/171)

Mangum, J. G., & Shirley, Y. L. 2015, *PASP*, 127, 266, doi: [10.1086/680323](https://doi.org/10.1086/680323)

Mangum, J. G., & Wootten, A. 1993, *ApJS*, 89, 123, doi: [10.1086/191841](https://doi.org/10.1086/191841)

Mangum, J. G., Wootten, A., & Mundy, L. G. 1992, *ApJ*, 388, 467, doi: [10.1086/171167](https://doi.org/10.1086/171167)

Mazumdar, P., Wyrowski, F., Colombo, D., et al. 2021, *A&A*, 650, A164, doi: [10.1051/0004-6361/202040205](https://doi.org/10.1051/0004-6361/202040205)

McKee, C. F., & Ostriker, E. C. 2007, *ARA&A*, 45, 565, doi: [10.1146/annurev.astro.45.051806.110602](https://doi.org/10.1146/annurev.astro.45.051806.110602)

Mendoza, E., Carvajal, M., Merello, M., Bronfman, L., & Boechat-Roberty, H. M. 2023, *ApJ*, 953, 77, doi: [10.3847/1538-4357/ace048](https://doi.org/10.3847/1538-4357/ace048)

Molinari, S., Merello, M., Elia, D., et al. 2016, *ApJL*, 826, L8, doi: [10.3847/2041-8205/826/1/L8](https://doi.org/10.3847/2041-8205/826/1/L8)

Müller, H. S. P., Schlöder, F., Stutzki, J., & Winnewisser, G. 2005, *Journal of Molecular Structure*, 742, 215, doi: [10.1016/j.molstruc.2005.01.027](https://doi.org/10.1016/j.molstruc.2005.01.027)

Müller, H. S. P., Thorwirth, S., Roth, D. A., & Winnewisser, G. 2001, *A&A*, 370, L49, doi: [10.1051/0004-6361:20010367](https://doi.org/10.1051/0004-6361:20010367)

Mundy, L. G., Evans, II, N. J., Snell, R. L., & Goldsmith, P. F. 1987, *ApJ*, 318, 392, doi: [10.1086/165376](https://doi.org/10.1086/165376)

Nagahama, T., Mizuno, A., Ogawa, H., & Fukui, Y. 1998, *AJ*, 116, 336, doi: [10.1086/300392](https://doi.org/10.1086/300392)

Park, G., Currie, M. J., Thomas, H. S., et al. 2023, *ApJS*, 264, 16, doi: [10.3847/1538-4365/ac9b59](https://doi.org/10.3847/1538-4365/ac9b59)

Pazukhin, A. G., Zinchenko, I. I., Trofimova, E. A., Henkel, C., & Semenov, D. A. 2023, *MNRAS*, 526, 3673, doi: [10.1093/mnras/stad2976](https://doi.org/10.1093/mnras/stad2976)

Reid, M. J., Myers, P. C., & Bieging, J. H. 1987, *ApJ*, 312, 830, doi: [10.1086/164929](https://doi.org/10.1086/164929)

Reid, M. J., Menten, K. M., Brunthaler, A., et al. 2014, *ApJ*, 783, 130, doi: [10.1088/0004-637X/783/2/130](https://doi.org/10.1088/0004-637X/783/2/130)

Santos, J. C., Bronfman, L., Mendoza, E., et al. 2022, *ApJ*, 925, 3, doi: [10.3847/1538-4357/ac36cc](https://doi.org/10.3847/1538-4357/ac36cc)

Schinnerer, E., & Leroy, A. K. 2024, *ARA&A*, 62, 369, doi: [10.1146/annurev-astro-071221-052651](https://doi.org/10.1146/annurev-astro-071221-052651)

Schneider, N., Motte, F., Bontemps, S., et al. 2010, *A&A*, 518, L83, doi: [10.1051/0004-6361/201014627](https://doi.org/10.1051/0004-6361/201014627)

Swift, J. J., Welch, W. J., & Di Francesco, J. 2005, *ApJ*, 620, 823, doi: [10.1086/427257](https://doi.org/10.1086/427257)

Tafalla, M., Myers, P. C., Caselli, P., & Walmsley, C. M. 2004, *A&A*, 416, 191, doi: [10.1051/0004-6361:20031704](https://doi.org/10.1051/0004-6361:20031704)

Tanaka, K., Ito, H., & Tanaka, T. 1987, *JChPh*, 87, 1557, doi: [10.1063/1.453725](https://doi.org/10.1063/1.453725)

Tang, X. D., Henkel, C., Chen, C.-H. R., et al. 2017, *A&A*, 600, A16, doi: [10.1051/0004-6361/201630183](https://doi.org/10.1051/0004-6361/201630183)

Tang, X. D., Henkel, C., Menten, K. M., et al. 2018, A&A, 609, A16, doi: [10.1051/0004-6361/201731849](https://doi.org/10.1051/0004-6361/201731849)

—. 2021, A&A, 655, A12, doi: [10.1051/0004-6361/202141804](https://doi.org/10.1051/0004-6361/202141804)

Tercero, F., López-Pérez, J. A., Gallego, J. D., et al. 2021, A&A, 645, A37, doi: [10.1051/0004-6361/202038701](https://doi.org/10.1051/0004-6361/202038701)

Torstensson, K. J. E., van der Tak, F. F. S., van Langevelde, H. J., Kristensen, L. E., & Vlemmings, W. H. T. 2011, A&A, 529, A32, doi: [10.1051/0004-6361/200913256](https://doi.org/10.1051/0004-6361/200913256)

Townes, C. H., & Schawlow, A. L. 1955, Microwave Spectroscopy (Mcgraw-Hill)

Tursun, K., Henkel, C., Esimbek, J., et al. 2022, A&A, 658, A34, doi: [10.1051/0004-6361/202141937](https://doi.org/10.1051/0004-6361/202141937)

Urquhart, J. S., Morgan, L. K., Figura, C. C., et al. 2011, MNRAS, 418, 1689, doi: [10.1111/j.1365-2966.2011.19594.x](https://doi.org/10.1111/j.1365-2966.2011.19594.x)

Urquhart, J. S., Figura, C. C., Moore, T. J. T., et al. 2015, MNRAS, 452, 4029, doi: [10.1093/mnras/stv1514](https://doi.org/10.1093/mnras/stv1514)

Virtanen, P., Gommers, R., Oliphant, T. E., et al. 2020, Nature Methods, 17, 261, doi: [10.1038/s41592-019-0686-2](https://doi.org/10.1038/s41592-019-0686-2)

Viti, S., & Williams, D. A. 1999, MNRAS, 305, 755, doi: [10.1046/j.1365-8711.1999.02447.x](https://doi.org/10.1046/j.1365-8711.1999.02447.x)

Wakelam, V., Smith, I. W. M., Herbst, E., et al. 2010, SSRv, 156, 13, doi: [10.1007/s11214-010-9712-5](https://doi.org/10.1007/s11214-010-9712-5)

Walmsley, C. M., & Ungerechts, H. 1983, A&A, 122, 164

Wienen, M., Wyrowski, F., Schuller, F., et al. 2012, A&A, 544, A146, doi: [10.1051/0004-6361/201118107](https://doi.org/10.1051/0004-6361/201118107)

Zhang, Q., Ho, P. T. P., & Ohashi, N. 1998, ApJ, 494, 636, doi: [10.1086/305243](https://doi.org/10.1086/305243)

Zhao, X., Tang, X. D., Henkel, C., et al. 2024, A&A, 687, A207, doi: [10.1051/0004-6361/202449352](https://doi.org/10.1051/0004-6361/202449352)

Table 1. Source list

Source Name	Alias	R.A. (J2000) (hh:mm:ss)	Decl. (J2000) (dd:mm:ss)	v_{LSR}^* (km s $^{-1}$)	D_{\odot}^{**} (kpc)	$K=2$ line of CH ₃ CCH 5-4 ***
G000.67-00.03	Sgr B2	17:47:20.00	-28:22:40.00	62 \pm 5	7.8	N
G005.88-00.39		18:00:30.31	-24:04:04.50	9 \pm 3	3.0	Y
G009.62+00.19		18:06:14.66	-20:31:31.70	2 \pm 3	5.2	Y
G010.47+00.02		18:08:38.23	-19:51:50.30	69 \pm 5	8.5	N
G010.62-00.38	W 31	18:10:28.55	-19:55:48.60	-3 \pm 5	5.0	Y
G011.49-01.48		18:16:22.13	-19:41:27.20	11 \pm 3	1.3	Y
G011.91-00.61		18:13:58.12	-18:54:20.30	37 \pm 5	3.4	Y
G012.02-00.03		18:12:01.84	-18:31:55.80	108 \pm 5	9.4	N
G012.68-00.18		18:13:54.75	-18:01:46.60	58 \pm 10	2.4	N
G012.80-00.20		18:14:14.23	-17:55:40.50	34 \pm 5	2.9	Y
G012.88+00.48	IRAS 18089-1732	18:11:51.42	-17:31:29.00	31 \pm 7	2.5	Y
G012.90-00.24		18:14:34.42	-17:51:51.90	36 \pm 10	2.5	Y
G012.90-00.26		18:14:39.57	-17:52:00.40	39 \pm 10	2.5	Y
G013.87+00.28		18:14:35.83	-16:45:35.90	48 \pm 10	3.9	Y
G014.33-00.64		18:18:54.67	-16:47:50.30	22 \pm 5	1.1	Y
G014.63-00.57		18:19:15.54	-16:29:45.80	19 \pm 5	1.8	Y
G015.03-00.67	M 17	18:20:24.81	-16:11:35.30	22 \pm 3	2.0	Y
G016.58-00.05		18:21:09.08	-14:31:48.80	60 \pm 5	3.6	Y
G023.00-00.41		18:34:40.20	-09:00:37.00	80 \pm 3	4.6	Y
G023.43-00.18		18:34:39.29	-08:31:25.40	97 \pm 3	5.9	Y
G023.65-00.12		18:34:51.59	-08:18:21.40	83 \pm 3	3.2	N
G023.70-00.19		18:35:12.36	-08:17:39.50	73 \pm 5	6.2	N
G025.70+00.04		18:38:03.14	-06:24:15.50	93 \pm 5	10.2	Y
G027.36-00.16		18:41:51.06	-05:01:43.40	92 \pm 3	8.0	Y
G028.86+00.06		18:43:46.22	-03:35:29.60	100 \pm 10	7.4	Y
G029.86-00.04		18:45:59.57	-02:45:06.70	100 \pm 3	6.2	N
G029.95-00.01	W 43S	18:46:03.74	-02:39:22.30	98 \pm 3	5.3	Y
G031.28+00.06		18:48:12.39	-01:26:30.70	109 \pm 3	4.3	Y
G031.58+00.07	W 43Main	18:48:41.68	-01:09:59.00	96 \pm 5	4.9	Y
G032.04+00.05		18:49:36.58	-00:45:46.90	97 \pm 5	5.2	Y
G033.64-00.22		18:53:32.56	+00:31:39.10	60 \pm 3	6.5	N
G034.39+00.22		18:53:19.00	+01:24:08.80	57 \pm 5	1.6	Y
G035.02+00.34		18:54:00.67	+02:01:19.20	52 \pm 5	2.3	Y
G035.19-00.74		18:58:13.05	+01:40:35.70	30 \pm 7	2.2	Y
G035.20-01.73		19:01:45.54	+01:13:32.50	42 \pm 3	3.3	N
G037.43+01.51		18:54:14.35	+04:41:41.70	41 \pm 3	1.9	Y
G043.16+00.01	W 49N	19:10:13.41	+09:06:12.80	10 \pm 5	11.1	N
G043.79-00.12	OH 43.8-0.1	19:11:53.99	+09:35:50.30	44 \pm 10	6.0	N

Table 1 *continued on next page*

Table 1 (*continued*)

Source Name	Alias	R.A. (J2000)	Decl. (J2000)	v_{LSR}^* (km s ⁻¹)	D_{\odot}^{**} (kpc)	<i>K</i> =2 line of CH ₃ CCH 5-4	***
		(hh:mm:ss)	(dd:mm:ss)				
G043.89-00.78		19:14:26.39	+09:22:36.50	54 ± 5	8.3	N	
G045.07+00.13		19:13:22.04	+10:50:53.30	59 ± 5	8.0	N	
G045.45+00.05		19:14:21.27	+11:09:15.90	55 ± 7	8.4	N	
G048.60+00.02		19:20:31.18	+13:55:25.20	18 ± 5	10.8	N	
G049.19-00.33		19:22:57.77	+14:16:10.00	67 ± 5	5.3	Y	
G049.48-00.36	W 51 IRS2	19:23:39.82	+14:31:05.00	56 ± 3	5.1	Y	
G049.48-00.38	W 51M	19:23:43.87	+14:30:29.50	58 ± 4	5.4	Y	
G052.10+01.04	IRAS 19213+1723	19:23:37.32	+17:29:10.50	42 ± 5	4.0	N	
G059.78+00.06		19:43:11.25	+23:44:03.30	25 ± 3	2.2	Y	
G069.54-00.97	ON 1	20:10:09.07	+31:31:36.00	12 ± 5	2.5	Y	
G074.03-01.71		20:25:07.11	+34:49:57.60	5 ± 5	1.6	Y	
G075.29+01.32		20:16:16.01	+37:35:45.80	-58 ± 5	9.3	N	
G075.76+00.33		20:21:41.09	+37:25:29.30	-9 ± 9	3.5	Y	
G075.78+00.34	ON 2N	20:21:44.01	+37:26:37.50	1 ± 5	3.8	Y	
G076.38-00.61		20:27:25.48	+37:22:48.50	-2 ± 5	1.3	Y	
G078.12+03.63	IRAS 20126+4104	20:14:26.07	+41:13:32.70	-4 ± 5	1.6	Y	
G078.88+00.70	AFGL 2591	20:29:24.82	+40:11:19.60	-6 ± 7	3.3	Y	
G079.73+00.99	IRAS 20290+4052	20:30:50.67	+41:02:27.50	-3 ± 5	1.4	Y	
G079.87+01.17		20:30:29.14	+41:15:53.60	-5 ± 10	1.6	Y	
G080.79-01.92	NML Cyg	20:46:25.54	+40:06:59.40	-3 ± 3	1.6	N	
G080.86+00.38	DR 20	20:37:00.96	+41:34:55.70	-3 ± 5	1.5	Y	
G081.75+00.59	DR 21	20:39:01.99	+42:24:59.30	-3 ± 3	1.5	Y	
G081.87+00.78	W 75N	20:38:36.43	+42:37:34.80	7 ± 3	1.3	Y	
G090.21+02.32		21:02:22.70	+50:03:08.30	-3 ± 5	0.7	N	
G092.67+03.07		21:09:21.73	+52:22:37.10	-5 ± 10	1.6	Y	
G094.60-01.79	AFGL 2789	21:39:58.27	+50:14:21.00	-46 ± 5	3.6	N	
G095.29-00.93		21:39:40.51	+51:20:32.80	-38 ± 5	4.9	N	
G097.53+03.18		21:32:12.43	+55:53:49.70	-73 ± 5	7.5	N	
G100.37-03.57		22:16:10.37	+52:21:34.10	-37 ± 10	3.4	N	
G105.41+09.87		21:43:06.48	+66:06:55.30	-10 ± 5	0.9	N	
G107.29+05.63	IRAS 22198+6336	22:21:26.73	+63:51:37.90	-11 ± 5	0.8	N	
G108.18+05.51	L 1206	22:28:51.41	+64:13:41.30	-11 ± 3	0.8	N	
G108.20+00.58		22:49:31.48	+59:55:42.00	-49 ± 5	4.4	N	
G108.47-02.81		23:02:32.08	+56:57:51.40	-54 ± 5	3.2	N	
G108.59+00.49		22:52:38.30	+60:00:52.00	-52 ± 5	2.5	N	
G109.87+02.11	Cep A	22:56:18.10	+62:01:49.50	-7 ± 5	0.7	Y	
G111.23-01.23		23:17:20.79	+59:28:47.00	-53 ± 10	3.5	N	
G111.25-00.76		23:16:10.36	+59:55:28.50	-43 ± 5	3.4	N	
G111.54+00.77	NGC 7538	23:13:45.36	+61:28:10.60	-57 ± 5	2.6	Y	
G121.29+00.65	L 1287	00:36:47.35	+63:29:02.20	-23 ± 5	0.9	Y	

Table 1 *continued on next page*

Table 1 (*continued*)

Source Name	Alias	R.A. (J2000) (hh:mm:ss)	Decl. (J2000) (dd:mm:ss)	v_{LSR} (km s $^{-1}$) [*]	D_{\odot} (kpc) ^{**}	$K=2$ line of CH ₃ CCH 5-4 ^{***}
G122.01-07.08	IRAS 00420+5530	00:44:58.40	+55:46:47.60	-50 \pm 5	2.2	N
G123.06-06.30	NGC 281	00:52:24.70	+56:33:50.50	-30 \pm 5	2.8	Y
G123.06-06.30	NGC 281W	00:52:24.20	+56:33:43.20	-29 \pm 3	2.4	Y
G133.94+01.06	W 3OH	02:27:03.82	+61:52:25.20	-47 \pm 3	2.0	Y
G134.62-02.19	S Per	02:22:51.71	+58:35:11.40	-39 \pm 5	2.4	N
G135.27+02.79	WB 89-437	02:43:28.57	+62:57:08.40	-72 \pm 3	6.0	N
G160.14+03.15		05:01:40.24	+47:07:19.00	-18 \pm 5	4.1	N
G168.06+00.82	IRAS 05137+3919	05:17:13.74	+39:22:19.90	-27 \pm 5	7.7	N
G176.51+00.20		05:37:52.14	+32:00:03.90	-17 \pm 5	1.0	Y
G182.67-03.26		05:39:28.42	+24:56:32.10	-7 \pm 10	6.7	N
G183.72-03.66		05:40:24.23	+23:50:54.70	3 \pm 5	1.8	Y
G188.79+01.03	IRAS 06061+2151	06:09:06.97	+21:50:41.40	-5 \pm 5	2.0	N
G188.94+00.88	S 252	06:08:53.35	+21:38:28.70	8 \pm 5	2.1	Y
G192.16-03.81		05:58:13.53	+16:31:58.90	5 \pm 5	1.5	Y
G192.60-00.04	S 255	06:12:54.02	+17:59:23.30	6 \pm 5	1.6	N
G196.45-01.67	S 269	06:14:37.08	+13:49:36.70	19 \pm 5	5.3	N
G209.00-19.38	Orion Nebula	05:35:15.80	-05:23:14.10	3 \pm 5	0.4	Y
G211.59+01.05		06:52:45.32	+01:40:23.10	45 \pm 5	4.4	N
G229.57+00.15		07:23:01.84	-14:41:32.80	47 \pm 10	4.5	N
G232.62+00.99		07:32:09.78	-16:58:12.80	21 \pm 3	1.7	N
G236.81+01.98		07:44:28.24	-20:08:30.20	43 \pm 7	3.4	N
G239.35-05.06	VY CMa	07:22:58.33	-25:46:03.10	20 \pm 3	1.2	N
G240.31+00.07		07:44:51.92	-24:07:41.50	67 \pm 5	4.7	N

*The v_{LSR} values are from Reid et al. (2014).

**The D_{\odot} values are derived from the trigonometric parallax reported in Reid et al. (2014).

***"Y" indicates that the CH₃CCH $K = 2$ line was detected above the 3σ level, while "N" denotes non-detection.

Table 2. The parameter of CH₃CCH $J=5-4$.

Transition $J_u, K_u - J_l, K_l$	Frequency (MHz)	A_{ul}^* (s ⁻¹)	g_u^*	E_u^* (K)	n_{crit}^{**} (cm ⁻³)
CH ₃ CCH 5,4-4,4	85431.17	7.30×10^{-7}	22	127.9	1.9×10^4
CH ₃ CCH 5,3-4,3	85442.60	1.30×10^{-6}	44	77.3	4.2×10^4
CH ₃ CCH 5,2-4,2	85450.77	1.70×10^{-6}	22	41.2	5.1×10^4
CH ₃ CCH 5,1-4,1	85455.67	1.94×10^{-6}	22	19.5	8.0×10^4
CH ₃ CCH 5,0-4,0	85457.30	2.03×10^{-6}	22	12.3	6.6×10^4

* Line spectroscopic parameters are given according to CDMS.

** The critical density of each transition is derived from the Einstein emission coefficient and collisional rate coefficients at 30 K given by EMAA.

Table 3. T_{rot} (CH₃CCH) and T_{rot} (2,2;1,1) used in this work

Source Name	$K=3$ line of CH ₃ CCH 5-4	*	T_{rot} (CH ₃ CCH)	T_{rot} (2,2;1,1)	Telescope	**
			(K)	(K)		
G005.88-00.39	Y		48.5 ± 0.4	27.9 ± 0.5	TMRT	
G009.62+00.19	Y		36.6 ± 0.3	25.2 ± 3.8	Effelsberg	
G010.62-00.38	Y		42.2 ± 0.3
G011.49-01.48	Y		26.9 ± 0.8	20.0 ± 0.6	TMRT	
G011.91-00.61	Y		26.3 ± 0.3	17.5 ± 0.4	TMRT	
G012.80-00.20	Y		44.4 ± 0.4
G012.88+00.48	Y		36.5 ± 0.4	19.3 ± 0.9	Effelsberg	
G012.90-00.24	N		30.2 ± 0.8	15.7 ± 0.4	TMRT	
G012.90-00.26	Y		34.7 ± 0.4	19.6 ± 0.6	Effelsberg	
G013.87+00.28	N		31.3 ± 0.7	22.3 ± 0.6	TMRT	
G014.33-00.64	Y		31.4 ± 0.3	21.3 ± 0.3	TMRT	
G014.63-00.57	Y		35.1 ± 0.5	18.4 ± 0.4	TMRT	
G015.03-00.67	Y		52.9 ± 0.8	28.2 ± 4.2	Effelsberg	
G016.58-00.05	N		26.5 ± 0.6	19.1 ± 0.8	Effelsberg	
G023.00-00.41	Y		29.9 ± 0.4	17.2 ± 0.5	Effelsberg	
G023.43-00.18	N		29.2 ± 0.6	20.0 ± 0.8	Effelsberg	
G025.70+00.04	N		23.0 ± 0.4	18.5 ± 1.1	Effelsberg	
G027.36-00.16	Y		28.1 ± 0.7	20.4 ± 0.5	TMRT	
G028.86+00.06	Y		37.9 ± 1.0	19.6 ± 0.9	TMRT	
G029.95-00.01	Y		24.1 ± 0.7	20.9 ± 1.0	Effelsberg	
G031.28+00.06	Y		40.9 ± 0.4	21.6 ± 1.1	Effelsberg	
G031.58+00.07	Y		32.1 ± 0.5	22.9 ± 0.6	TMRT	
G032.04+00.05	Y		33.0 ± 0.6	19.9 ± 0.3	TMRT	
G034.39+00.22	Y		36.9 ± 0.8	18.3 ± 0.3	TMRT	
G035.02+00.34	Y		33.1 ± 0.6	24.5 ± 0.8	TMRT	
G035.19-00.74	Y		34.9 ± 0.3	20.7 ± 0.5	Effelsberg	
G037.43+01.51	N		88.8 ± 3.0	21.9 ± 0.6	TMRT	
G049.19-00.33	N		42.1 ± 2.6	21.2 ± 1.0	TMRT	

Table 3 continued on next page

Table 3 (*continued*)

Source Name	$K=3$ line of CH_3CCH 5-4	* $T_{\text{rot}}(\text{CH}_3\text{CCH})$		Telescope
		(K)	(K)	
G049.48-00.36	Y	42.1 ± 0.4	25.2 ± 1.8	Effelsberg
G049.48-00.38	Y	48.6 ± 0.4	29.5 ± 0.6	Effelsberg
G059.78+00.06	Y	49.7 ± 0.9	19.1 ± 0.3	TMRT
G069.54-00.97	Y	29.5 ± 0.3	18.8 ± 3.4	Effelsberg
G074.03-01.71	N	33.4 ± 0.7	16.7 ± 0.4	TMRT
G075.76+00.33	Y	43.9 ± 0.6	26.4 ± 0.5	TMRT
G075.78+00.34	Y	41.7 ± 0.7	24.2 ± 0.5	TMRT
G076.38-00.61	Y	54.5 ± 1.6	23.7 ± 0.7	TMRT
G078.12+03.63	N	32.0 ± 1.0	18.5 ± 0.7	Effelsberg
G078.88+00.70	Y	26.9 ± 0.8	27.5 ± 0.6	TMRT
G079.73+00.99	N	29.2 ± 1.1	17.9 ± 0.7	TMRT
G079.87+01.17	N	26.6 ± 0.8	22.7 ± 1.1	TMRT
G080.86+00.38	N	32.5 ± 1.4	23.4 ± 0.5	TMRT
G081.75+00.59	Y	31.3 ± 0.3	18.5 ± 0.3	Effelsberg
G081.87+00.78	Y	30.4 ± 0.5	25.2 ± 0.4	TMRT
G092.67+03.07	Y	38.3 ± 0.6	24.5 ± 0.6	TMRT
G109.87+02.11	Y	36.1 ± 0.4	23.2 ± 3.0	Effelsberg
G111.54+00.77	N	43.1 ± 0.9	26.0 ± 1.3	Effelsberg
G121.29+00.65	N	25.2 ± 0.9	18.1 ± 0.2	TMRT
G123.06-06.30	N	27.1 ± 1.0	21.5 ± 0.5	TMRT
G123.06-06.30	Y	37.1 ± 1.2	20.1 ± 0.5	TMRT
G133.94+01.06	Y	38.1 ± 0.8
G176.51+00.20	N	49.6 ± 1.9	17.6 ± 0.4	TMRT
G183.72-03.66	N	31.6 ± 1.1	17.5 ± 0.4	TMRT
G188.94+00.88	N	31.2 ± 0.9	22.3 ± 0.4	TMRT
G192.60-00.04	N	46.4 ± 1.1	17.4 ± 1.5	TMRT
G209.00-19.38	Y	38.1 ± 0.7

* "Y" indicates that the CH_3CCH $K = 2$ line was detected above the 3σ level, while "N" denotes non-detection.

**Telescope using TMRT indicates NH_3 data obtained in this work. The telescope using Effelsberg indicates NH_3 data are taken from (Li et al. 2016a). Please note that G010.62-00.38, G012.80-00.20, G133.94+01.06 and G209.00-19.38 have no NH_3 data because of the absorption or low signal-to-noise ratio.

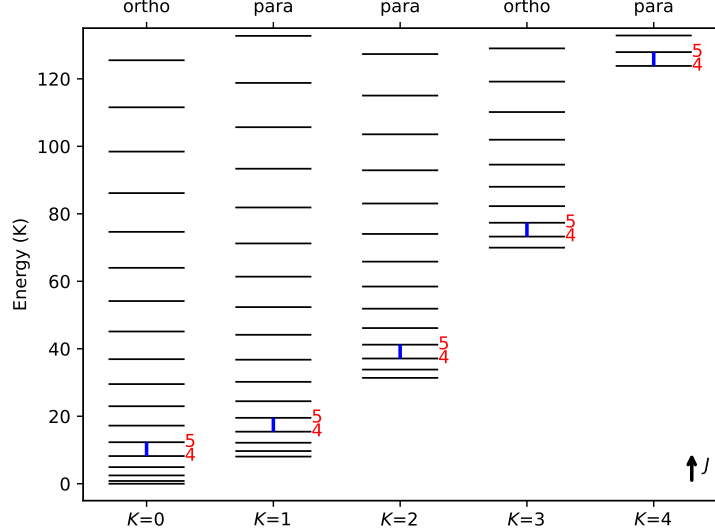


Figure 1. Energy levels of CH₃CCH. The nuclear spin symmetries and their “para” and “ortho” appellations are indicated. The blue line between two levels indicates the $J = 5 - 4$ transitions, which are used in this work. The level energies were obtained from CDMS.

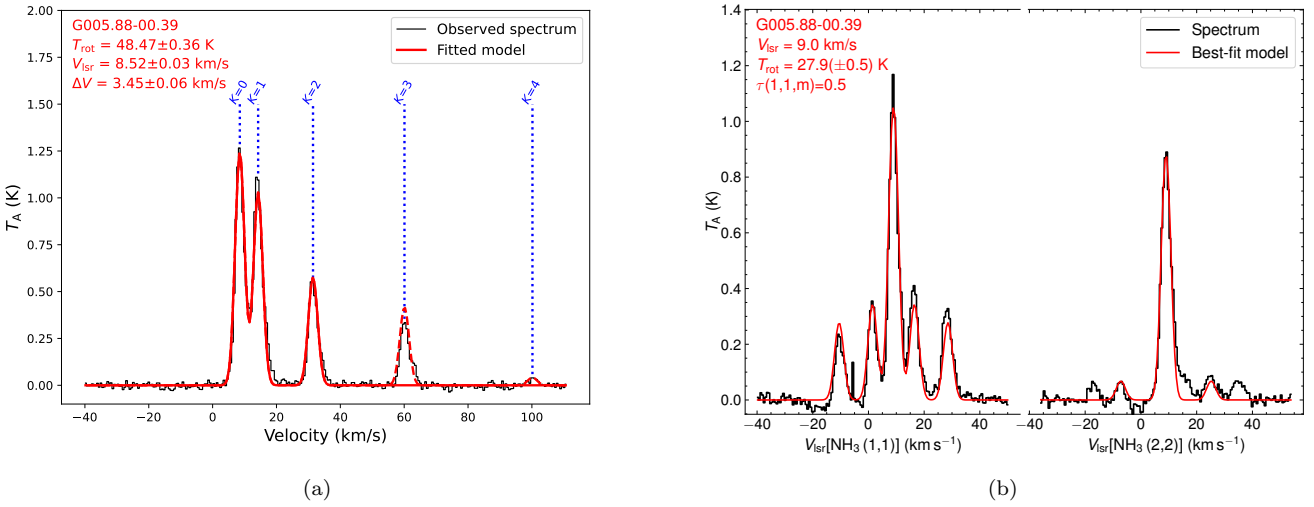


Figure 2. (a) The CH₃CCH $J=5-4$ fitting result in G005.88-00.39. The observed spectra are in black, while the red is the best fit from our code. The red dashed line indicates the expected line of the $K = 3, 4$ transition. (b) The spectra of NH₃(1,1) and NH₃(2,2) in G005.88-00.39. The observed spectra are in black, while the red are the best fit from the code of Lu et al. (2015).

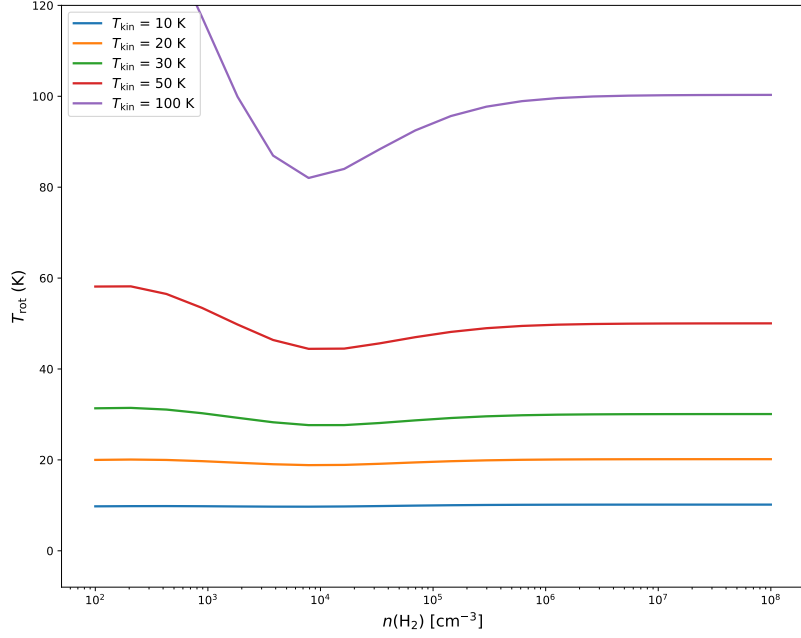


Figure 3. $\text{CH}_3\text{CCH } J=5-4, K=0,1,2,3,4$ rotation temperature as a function of temperature and density.

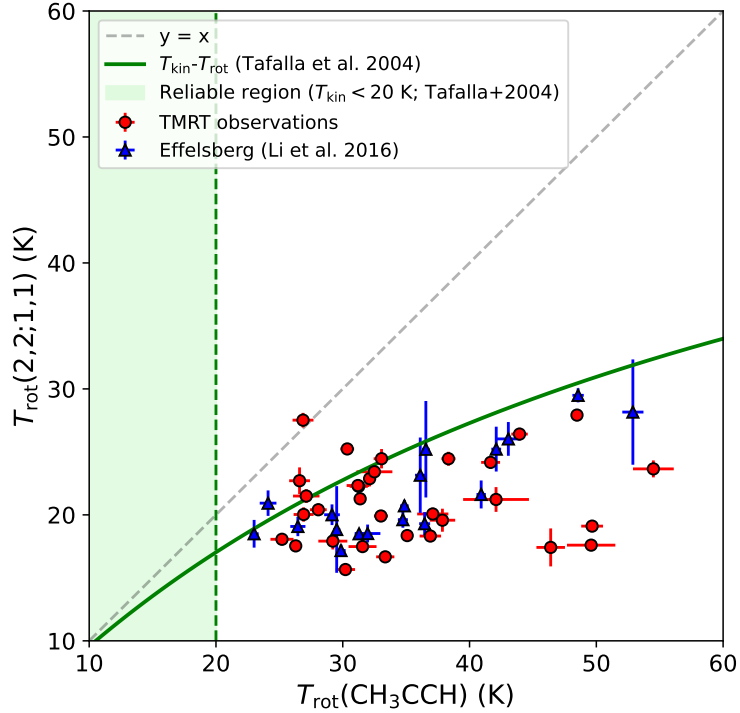


Figure 4. Comparison between T_{rot} derived from CH_3CCH and T_{rot} derived from NH_3 . Each point represents one source. The red circles correspond to NH_3 data observed with TMRT in this work, while the blue triangles are NH_3 data from Li et al. (2016a) observed with the Effelsberg. The x-axis shows the rotation temperature derived from CH_3CCH , and the y-axis shows that derived from NH_3 . The green curve represents the relation between $T_{\text{rot}}(2,2;1,1)$ and T_{kin} derived by Tafalla et al. (2004), and the light-green shaded area marks the reliable temperature range reported in that work.

APPENDIX

A. THE SOURCES WITH NOTABLE TEMPERATURE DIFFERENCES BETWEEN $T_{\text{ROT}}(\text{CH}_3\text{CCH})$ AND $T_{\text{ROT}}(2,2;1,1)$

Among 51 sources used in this work, five show departures from the overall consistency between $T_{\text{rot}}(\text{CH}_3\text{CCH})$ and $T_{\text{rot}}(2,2;1,1)$. Only one source, G078.88+00.70, shows a case where the rotation temperature derived from CH₃CCH ($T_{\text{rot}}(\text{CH}_3\text{CCH})$) is slightly lower (0.6 K) than that from NH₃(1,1)&(2,2) ($T_{\text{rot}}(2,2;1,1)$). This indicates that the two temperatures are consistent within the uncertainties. One exceptional case is G037.43+01.51, which shows an unusually high $T_{\text{rot}}(\text{CH}_3\text{CCH})$ of 88.8 K. However, since the CH₃CCH $K=2$ transition in this source was only marginally detected, the temperature estimate was unreliable. Therefore, we exclude this source in our analysis. There are three other notable sources, G059.78+00.06, G176.51+00.20, and G192.60-00.04, which show significantly higher $T_{\text{rot}}(\text{CH}_3\text{CCH})$ compared to $T_{\text{rot}}(2,2;1,1)$. In G176.51+00.20, the CH₃CCH $K=2$ transition was marginally detected, which may affect the reliability of the CH₃CCH temperature estimate. In G192.60-00.04, the NH₃(2,2) was marginally detected, likely leading to an underestimated $T_{\text{rot}}(2,2;1,1)$. As for G059.78+00.06, the discrepancy might also arise from general observational uncertainties between TMRT and Yebes affecting either or both calculations.

B. THE FITTING RESULT OF CH₃CCH 5-4

We present the fitting result of CH₃CCH 5-4.

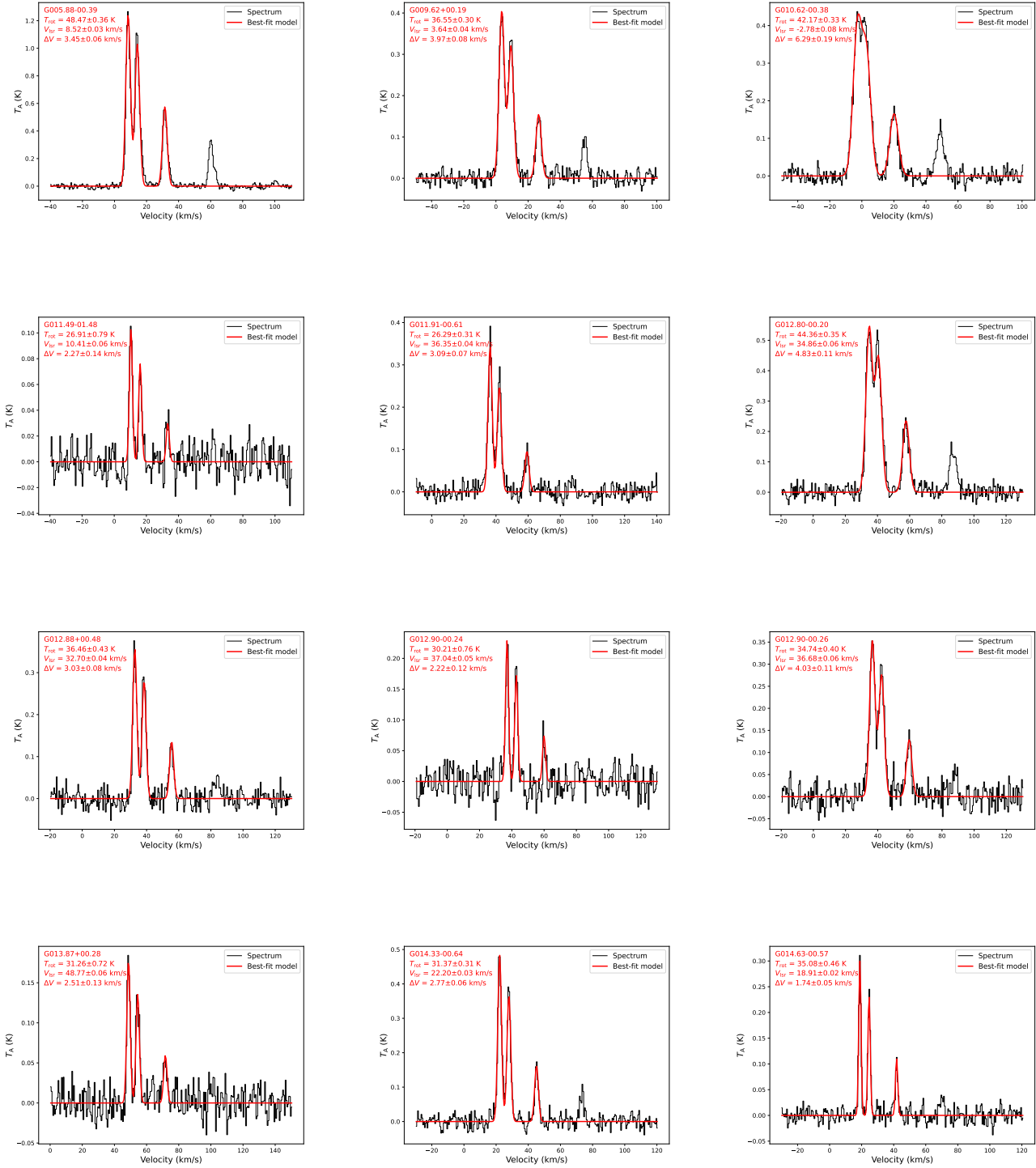


Figure B1. CH₃CCH spectra toward the sample sources (1/6). The observed spectra of CH₃CCH 5-4 are in black, while the best fit is in red.

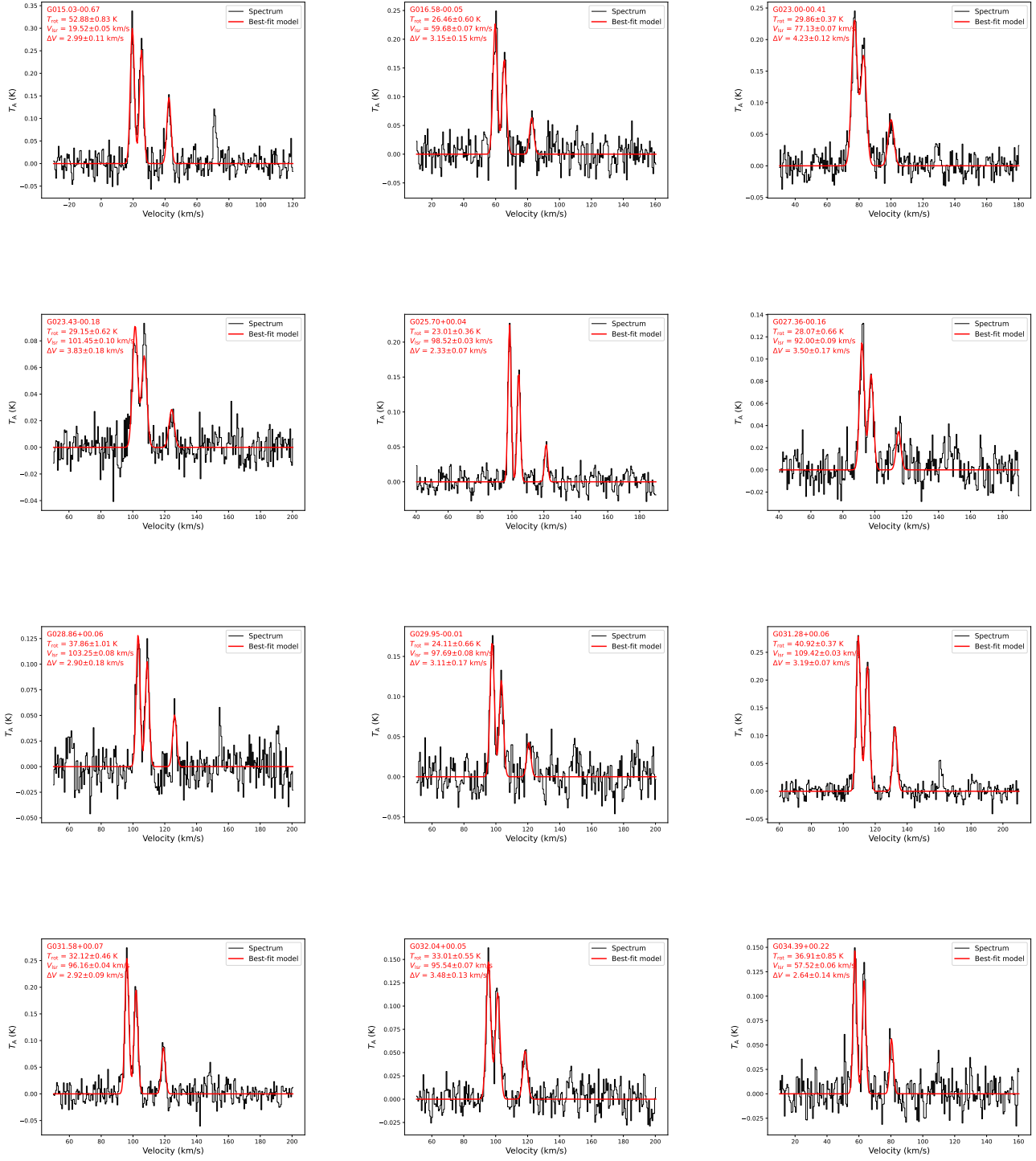


Figure B2. CH₃CCH spectra toward the sample sources (2/6). The observed spectra of CH₃CCH 5-4 are in black, while the best fit is in red.

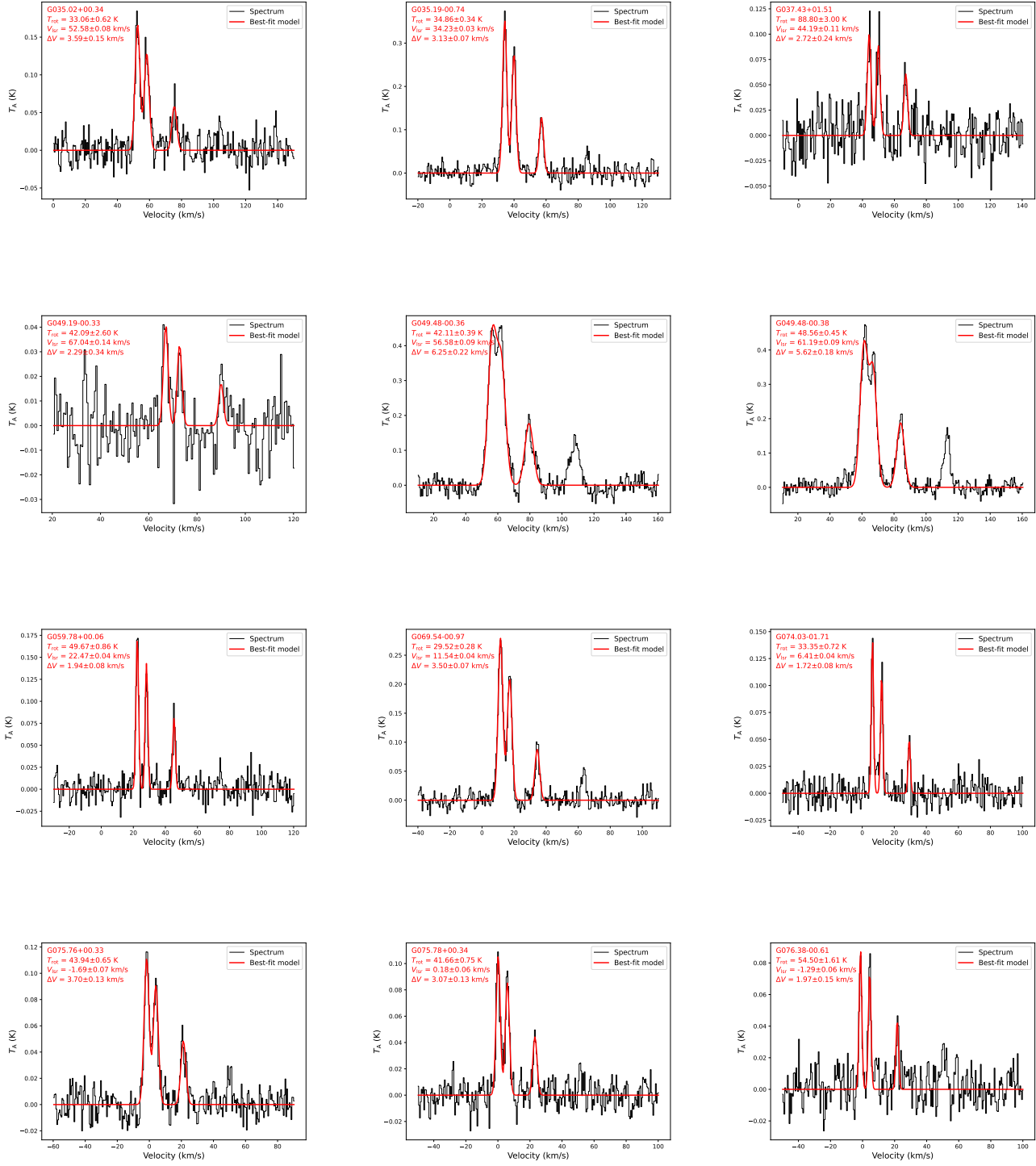


Figure B3. CH₃CCH spectra toward the sample sources (3/6). The observed spectra of CH₃CCH 5-4 are in black, while the best fit is in red.

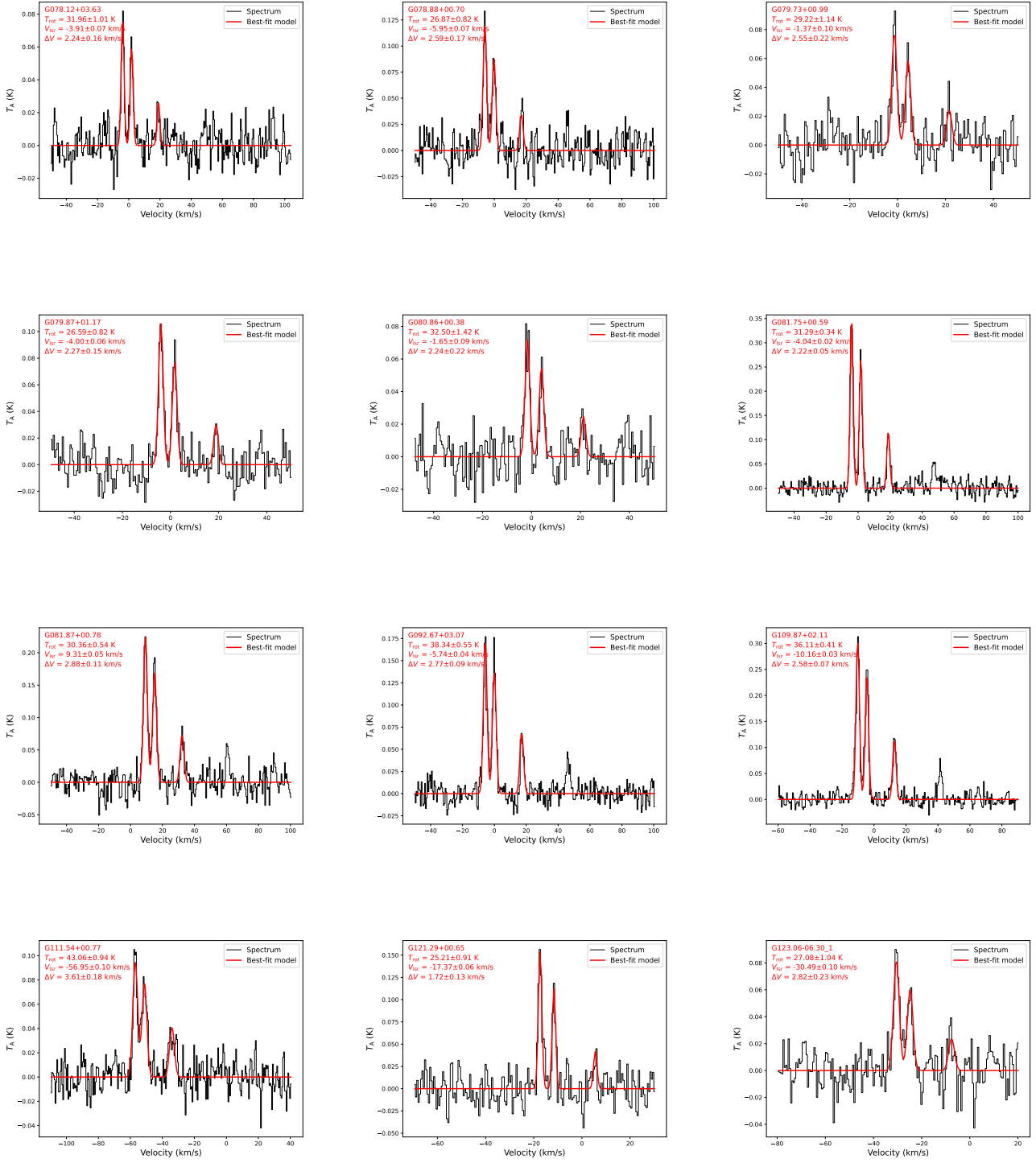


Figure B4. CH₃CCH spectra toward the sample sources (4/6). The observed spectra of CH₃CCH 5-4 are in black, while the best fit is in red.

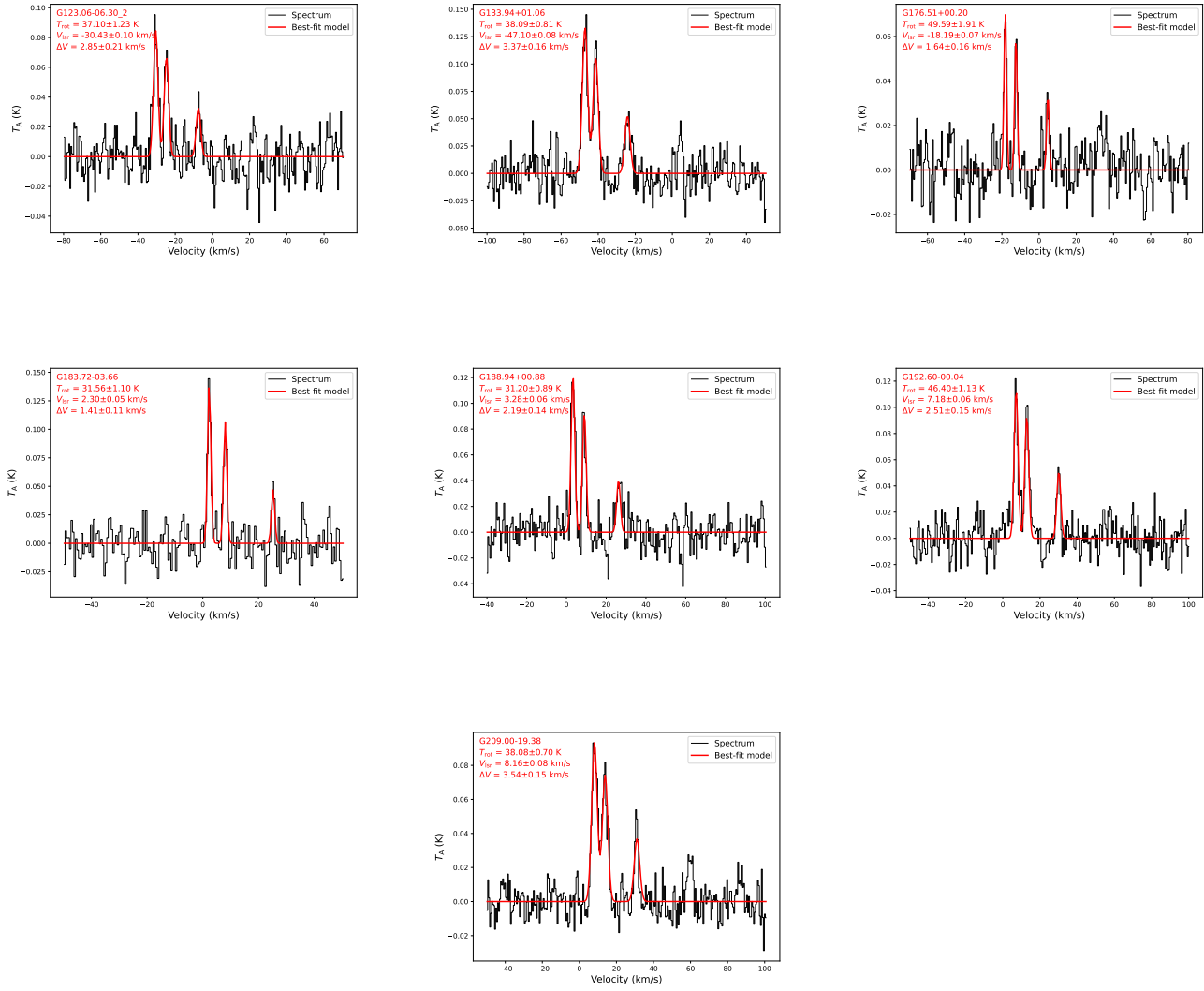


Figure B5. CH₃CCH spectra toward the sample sources (5/6). The observed spectra of CH₃CCH 5-4 are in black, while the best fit is in red.

C. THE FITTING RESULT OF NH₃

We present the fitting result of NH₃(1,1) and NH₃(2,2).

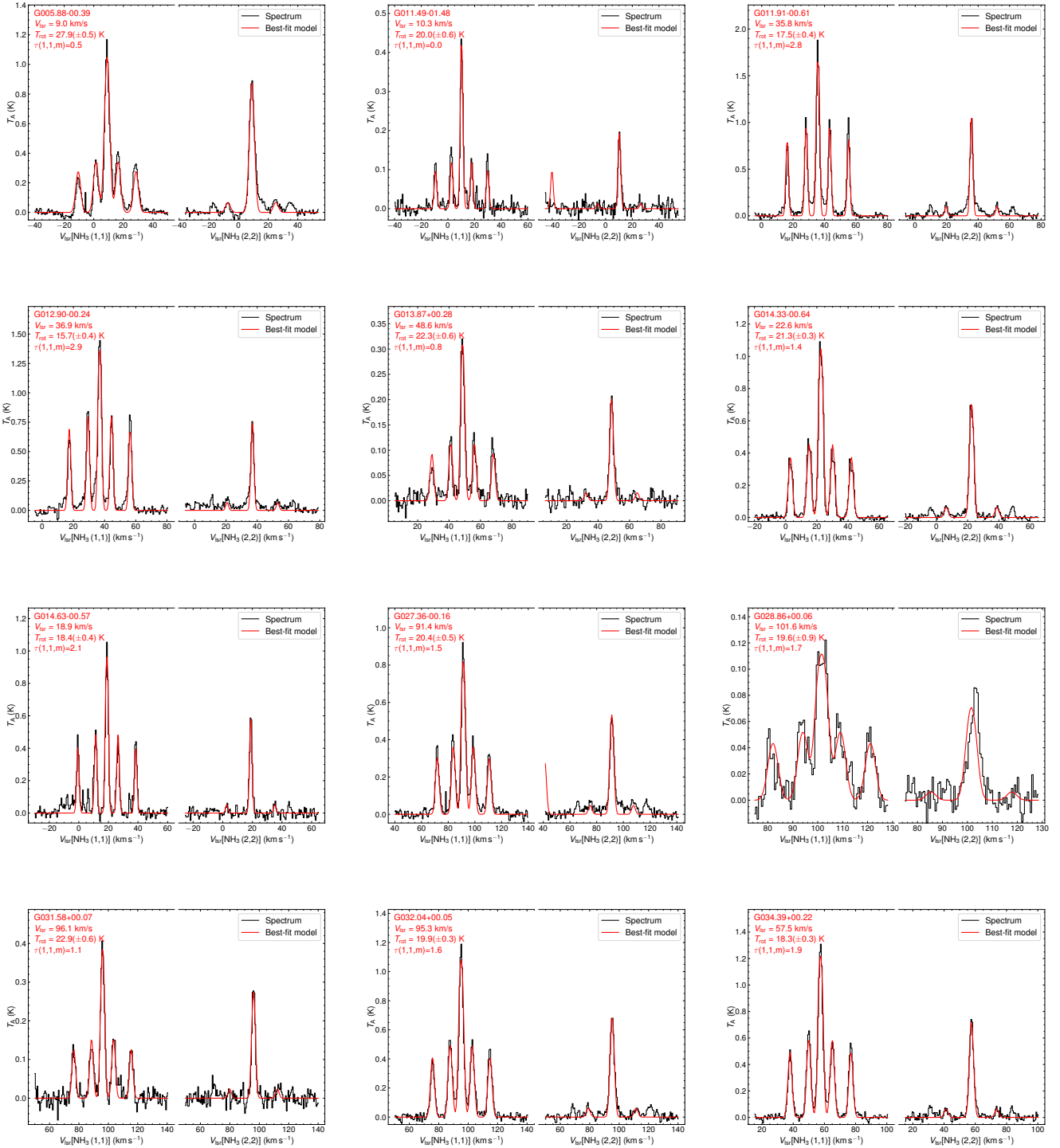


Figure C1. NH₃ spectra toward the sample sources (1/2). The observed spectra of NH₃(1,1) and NH₃(2,2) are in black, while the best fit from the code of Lu et al. (2015) is in red.

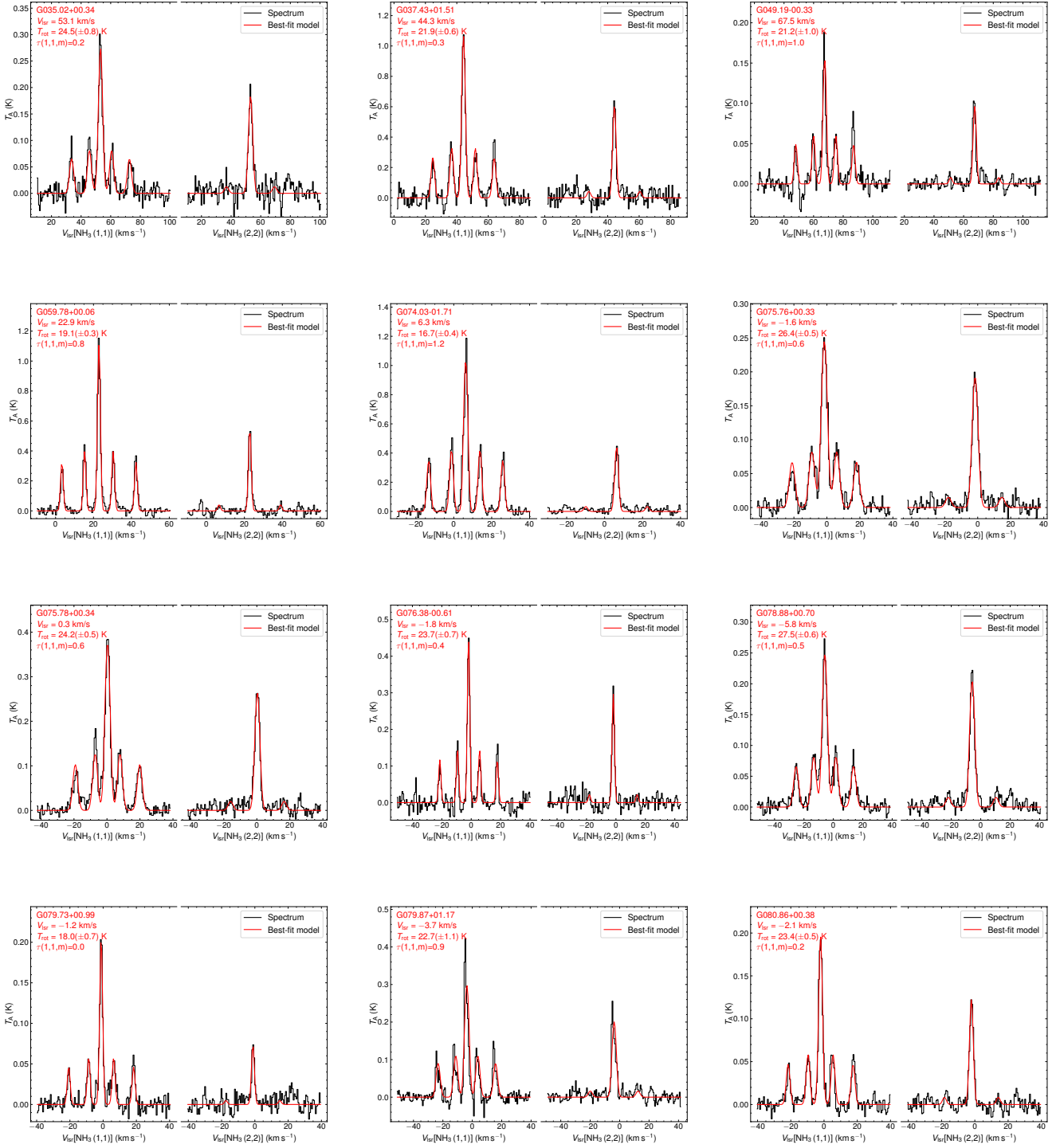


Figure C2. NH_3 spectra toward the sample sources (2/2). The observed spectra of $\text{NH}_3(1,1)$ and $\text{NH}_3(2,2)$ are in black, while the best fit from the code of Lu et al. (2015) is in red.

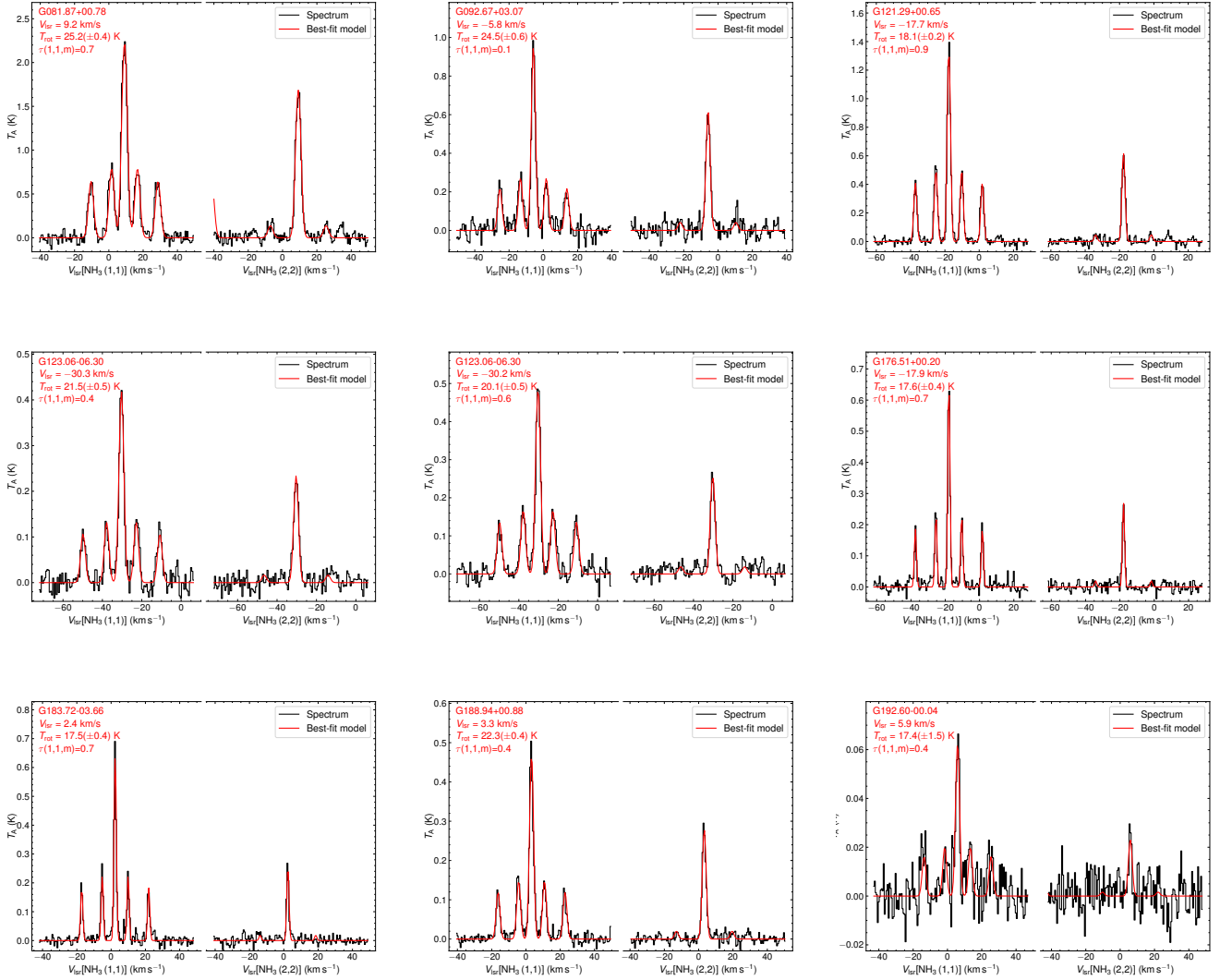


Figure C3. NH₃ spectra toward the sample sources (3/3). The observed spectra of NH₃(1,1) and NH₃(2,2) are in black, while the best fit from the code of Lu et al. (2015) is in red.

D. CHECKING THE CH₃CCH FITTING PROGRAM

We used the SciPy Python package to fit the CH₃CCH $J=5-4$ spectra and derive the T_{rot} (CH₃CCH). To ensure the reliability of derived rotation temperatures, we conducted the following tests, which are summarized below.

Comparison between fits with and without including the $K=3$ transition. We fit the CH₃CCH $J=5-4$ using $K=0,1,2$ transitions in our targets, because the $K=3$ transition was not detected in some sources. To assess whether the inclusion of the $K=3$ transition significantly affects the derived T_{rot} , we selected three sources where the $K=3$ line was clearly detected and compared the fitting results with and without this transition. As shown in Figure D1, the T_{rot} derived with and without $K=3$ are generally consistent, except for G005.88-00.39. This target has been reported to show a strong H¹³CN 1-0 emission ($\int T_{\text{mb}} d\nu \geq 40$ K km s⁻¹, Li et al. (2024)) with IRAM 30m observations, indicating that the gas density is extremely high. In this target, CH₃CCH is more likely to be optically thick, especially in the low K transitions. Therefore, this discrepancy is likely due to the high column density and volume density in G005.88-00.39, which may cause the lower- K transitions ($K=0$ and 1) to become optically thick. This optical depth effect flattens the population distribution of the low- K levels and consequently leads to an overestimated T_{rot} (CH₃CCH) (Goldsmith & Langer 1999).

Comparison between the rotational diagram method and Python fitting results. The rotational diagram method is often used to derive the T_{rot} from multiple transitions. Our Python program follows a similar theoretical framework with the rotational diagram method to derive T_{rot} . To validate the reliability of our code, we compared the T_{rot} obtained from our Python fitting with those derived from the rotational diagram method (see Figure D2). The two methods yield consistent T_{rot} , confirming that the theoretical implementation in our code is accurate.

Is the simulated result for the non-detected line consistent with the noise level? To test the reliability of our fitting results in cases where the CH₃CCH $J=5-4$ $K=3$ was not detected, we selected three sources in which CH₃CCH $J=5-4$ $K=3$ was not detected. If the simulated peak intensity of the $K=3$ transition is below the observed noise level, it confirms the correctness of the fitting result. As shown in Figure D3, the simulated $K=3$ peaks lie below the corresponding 3σ level in the observed spectra, supporting the validity of our fitting approach.

These tests confirm the internal consistency of our CH₃CCH fitting results.

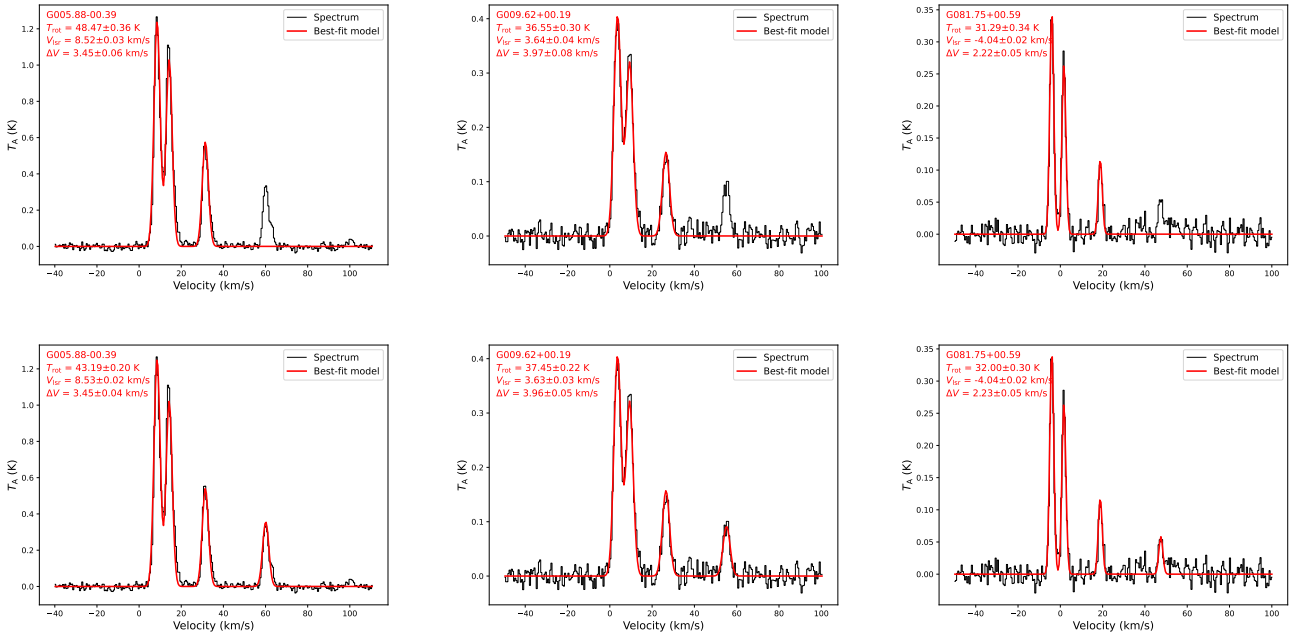


Figure D1. The upper panel shows fitting results of CH₃CCH $J=5-4$ not considering $K=3$, while the bottom panel considers $K=3$.

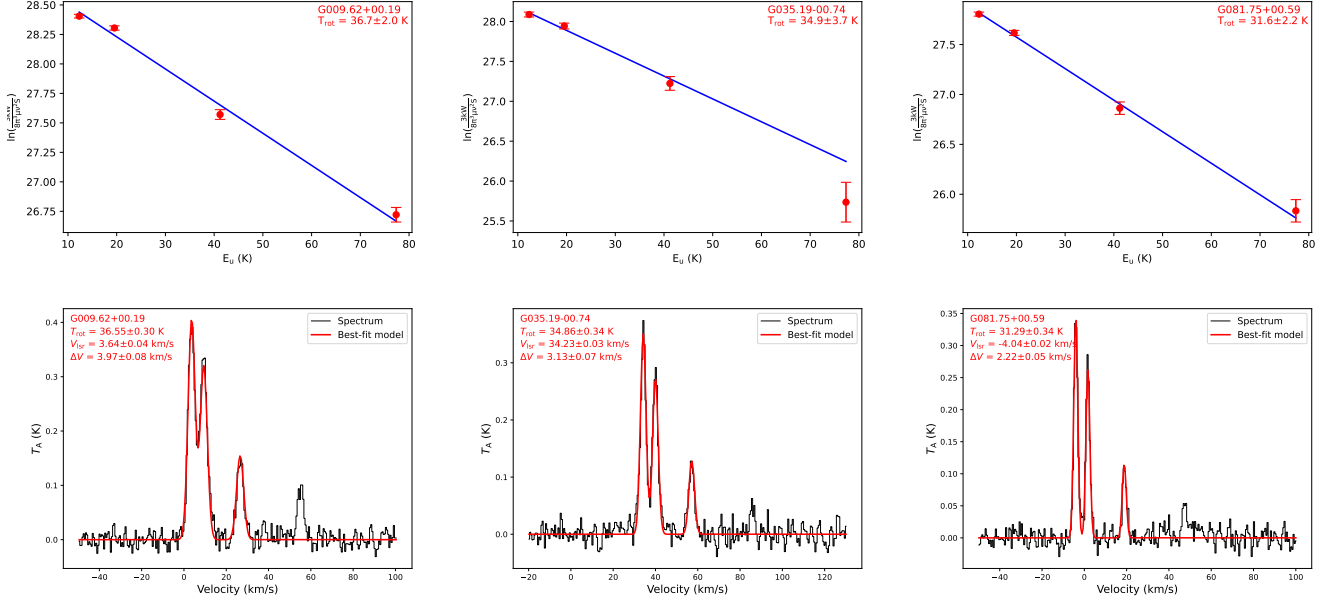


Figure D2. The upper panel shows the rotation diagrams of CH₃CCH $J=5-4$. Although four K -ladder transitions are displayed in the rotation diagrams, only the $K=0, 1$, and 2 transitions were used to derive the rotation temperatures. In order to retain all the observational information and comparison, the $K=3$ line is also included. The intensities are given in T_{A} , so the derived rotation temperatures are unchanged, but the column densities should be corrected by the main beam efficiency to obtain the true values. The bottom panel shows the fitting results of CH₃CCH $J=5-4$ corresponding to the upper panel source.

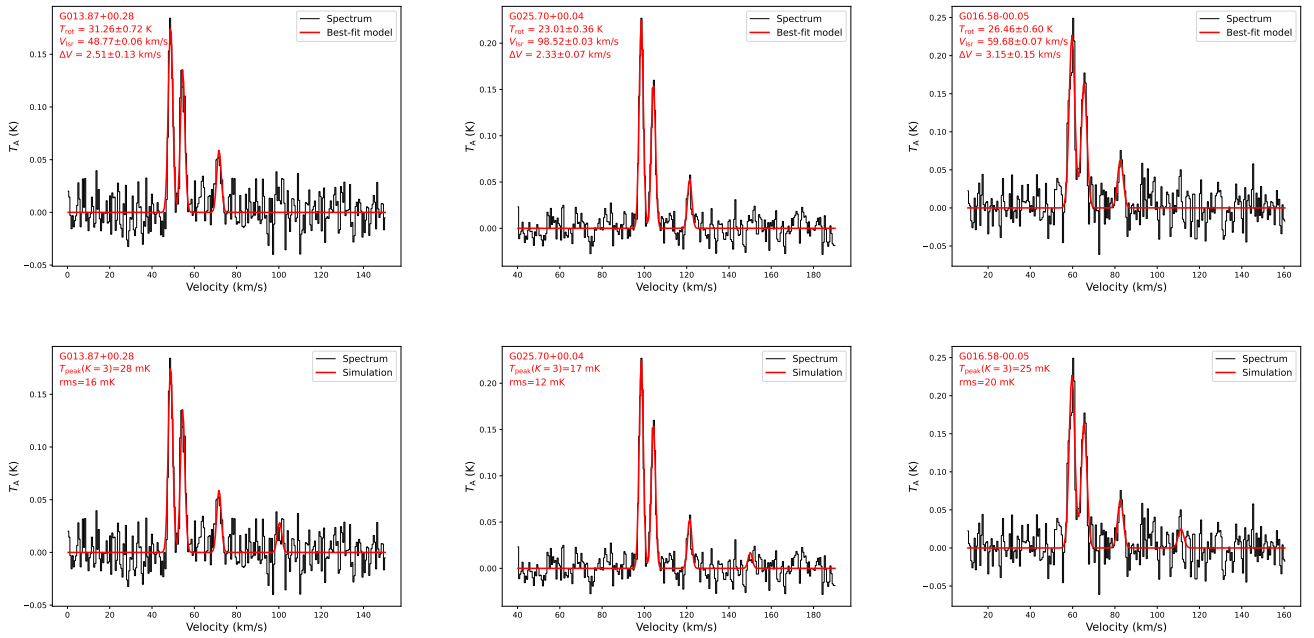


Figure D3. The upper panel shows the fitting results of CH₃CCH $J=5-4$, while the bottom panel shows the spectra and the simulation results.